國 立 交 通 大 學

電子工程學系　電子研究所碩士班

碩 士 論 文

矽基片雙抗諧振反射光波導結構分光元件之
設計、研製與特性量測
Design, Fabrication, and Characterization of
Si-Based Dual ARROW Power Splitters

研 究 生 ：許茗舜　　　　Ming-Shun Hsu

指導教授 ：黃遠東 博士　　Dr. Yang-Tung Huang

中華民國 一○○ 年 四 月

矽基片雙抗諧振反射光波導結構分光元件之
設計、研製與特性量測
Design, Fabrication, and Characterization of
Si-Based Dual ARROW Power Splitters

研 究 生：許茗舜　　　　Student: Ming-Shun Hsu

指導教授：黃遠東 博士　　Advisor: Dr. Yang-Tung Huang

國立交通大學

電子工程學系　　　電子研究所碩士班

碩 士 論 文

A Thesis
Submitted to Department of Electronics Engineering and Institute of
Electronics College of Electrical and Computer Engineering
National Chiao Tung University
in Partial Fulfillment of the Requirements
for the Degree of Master
in
Electronics Engineering
April 2011
Hsinchu, Taiwan, Republic of China

中 華 民 國 一○○ 年 四 月

矽基片雙抗諧振反射光波導結構分光元件之設計、研製與特性量測

研究生: 許茗舜　　　　　　　　指導教授: 黃遠東 博士

國立交通大學

電子工程學系　　電子研究所碩士班

摘 要

　　本論文研究矽基片雙抗諧振反射光波導結構分光元件之設計、製作與特性量測，不同耦合長度分光元件的性能亦被探討。對於一個抗諧振反射光波導結構而言，光場藉由在各層之間抗諧振條件被限制於核心層，而在空氣與導光區的界面則藉由全反射來限制。且其可具有較厚的導光區與較低的折射率與單模光纖匹配，因此可有效地與單模光纖耦合。此外，雙抗諧振反射光波導間之耦合效率可以利用調整結構對稱性來控制，因此可依不同需求，設計出符合所需的元件結構。在此研究中，我們利用轉移矩陣法和等效折射係數法來分析及設計抗諧振反射光波導之結構，然後利用波束傳輸法來模擬雙抗諧振反射光波導分光元件之傳輸特性。設計元件兩波導間距為30微米，其耦合長度為4300微米。我們實作元件，其耦合區域長度為1950、2050、2150（半耦合長度）、2250及2350微米，並加以量測特性。雙抗諧振反射光波導分光元件量測結果如下：從左邊波導輸入之兩波導輸出之不均勻度差及標準差平均為0.45 dB及0.12 dB，而從右邊波導輸入之值則分別為0.57 dB及0.05 dB。耦合區域長度為2150微米的五個樣品從左邊波導輸入之傳輸損耗分別為3.45、1.95、2.33、1.51及1.88 dB/cm，而從右邊波導輸入之值則分別為2.98、1.27、1.55、2.08及1.84 dB/cm。雙抗諧振反射光波導分光元件製作結果之特性量測，顯示其可有效地分光。

Design, Fabrication, and Characterization of Si-Based Dual ARROW Power Splitters

Student: Ming-Shun Hsu   Advisor: Dr. Yang-Tung Huang

Department of Electronics Engineering

and Institute of Electronics

National Chiao Tung University

ABSTRACT

In this thesis, design, fabrication, and characterization of Si-based dual ARROW power splitters are investigated, and the performances of the power splitters with different lengths of the coupling region are presented. For an ARROW structure, light is confined within the core layer by antiresonance conditions in the cladding layers and by total internal reflection at the air-core interface, and it can guide waves in low-index cores with a large core size such that their core index and size can be compatible with single-mode fiber index and diameter to provide efficient coupling with fibers. Moreover, a dual ARROW waveguide can operate as a directional coupler or as two decoupled waveguides by controlling the structural symmetry. Dual ARROW power splitters were realized with ARROW structure in the vertical and horizontal directions. We analyzed and designed ARROW structure with the transfer matrix method (TMM) and the effective index method (EIM). Then, we used the beam propagation method (BPM) to simulate the propagation characteristics of the dual ARROW power splitter. In our devices, we designed the dual ARROW power splitter with a separation width of 30 μm and the coupling length L_c is 4300 μm. We fabricated the devices with the lengths of the coupling region as 1950, 2050, 2150 ($L_c/2$), 2250, and 2350 μm to verify the design idea. The average imbalance and standard deviation are 0.45 and 0.12 dB by launching a power into the left core of five samples, and 0.57 and 0.05 dB for launching a power into the right core. The propagation losses of five samples for the length of the coupling region as 2150 μm by launching a power into the left core are 3.45, 1.95, 2.33, 1.51, and 1.88 dB/cm, and for the right core are 2.98, 1.27, 1.55, 2.08, and 1.84 dB/cm. Measurement results show that our dual ARROW power splitters can be efficiently realized.

Acknowledgement

First of all, I feel an immense gratitude to my advisor, Prof. Yang-Tung Huang, for his guidance on my research as well as studies, and for his support in every way. He always kindly corrects my mistakes and ignorance, and is full of enthusiasm and inspiration. He can always use the example which extrapolates to cause us understand questions easily. His ideas and advices help me correct many errors. Even though he is busy, but he still spends time to instruct our researches.

Moreover, I appreciate Jian-Hua Chen. He helped me to learn a lot of simulation tools and related research knowledge, and gave me many helps of operating instruments in the National Nano Device Laboratories. I also would like to express my appreciation to Ting-Yu Qiu, Zhi-Xiang Yang, Shu-Wei Chang, Jian-Wei Cheng, Cang-Xian Su, Hsin-Feng Hsu, and other members in our laboratory brought me lots of happiness for two years. They enable me to complete my thesis on schedule propitiously under theirs surveillance.

Finally, I am sincerely indebted to my family and others concerned about me, for their support and encouragement, and this dissertation is dedicated to my parents.

Contents

List of Tables

List of Figures

Chapter 1

Introduction

Power splitters are important integrated optical components. By using standard semi-conductor fabrication process, they offer the possibility of fabricating multiple devices on a single chip and the prospect of integrating optical and electrical functions to form a smart system. For conventional dual waveguides, the coupling strength is decreasing as an exponential function of the waveguide separation. Many coupling problems are analyzed based on the coupled mode theory with weakly coupled approximations [1]-[5].

In comparison with core size, there is a large difference between connection fibers and conventional waveguides such as to generate a serious coupling problem. Therefore, efficient fiber-waveguide coupling as well as low waveguide propagation loss are essential, and many researchers are devoted to alignment technology of fiber-waveguide. In contrast to conventional waveguides, antiresonant reflecting optical waveguides (ARROW) have been proposed and demonstrated [6]. ARROW structures can guide waves in low-index cores with a large core size on a high-index substrate, such that their core index and size can be compatible with single-mode fiber index and diameter to provide efficient coupling to fibers.

For power splitters, there are different ways to equally split the power of incoming signals into two output ports with an equal power: for example, using a symmetric Y-junction structures or based on conventional directional couplers. The wide separation between the output waveguides requires a bending structure for the signal to be split. Although 1×2 multimode interference (MMI) coupler [7] can shorten the device length efficiently, but it also requires a large spacing. In this regard, one might consider employing remote couplers such as couplers based on ARROW structures [8].

A directional coupler consisting of two identical ARROW's was recently proposed [8]. The main advantage of an ARROW-based coupler over a conventional waveguide coupler is that ARROW's can be remotely coupled because of their nondecaying field profile inside the intermediate cladding layers. They are suitable for such stacked interconnects, and similar dual ARROW structure has been demonstrated in 1988 [9, 10]. Here, we investigated power splitters based on a dual ARROW structure. The widths and the thicknesses of the intermediate cladding layers were designed to achieve large fabrication tolerance and a short coupling length. Finally, the dual ARROW power splitters were demonstrated.

The organization of this thesis is as follows. In Chapter 2, several analytic methods for integrated optical waveguides are briefly reviewed, which include the transfer matrix method (TMM) [11], the effective index method (EIM) [12], and the beam propagation method (BPM) [13]. In Chapter 3, basic characteristics of an ARROW structures are briefly discussed. The dual ARROW power splitters were designed based on these theories. In Chapter 4, the fabrication process of the dual ARROW power splitters and the parameters of the fabrication process are introduced. After all of the fabrication process were accomplished, the measurement system at an operating wavelength λ of 1.55 μm was established, and the measurement results of the dual ARROW power splitters are discussed in Chapter 5. In Chapter 6, the discussions and conclusions of our dual ARROW power splitters are given.

Chapter 2

Analytic Theories and Methods

2.1 Introduction

In this chapter, several methods of analyzing integrated optical waveguides are briefly reviewed. First, for solving the dispersion relation of a multilayer slab waveguide, the transfer matrix method is derived [11]. Second, for analyzing a three-dimensional (3-D) optical waveguide structure simply, the effective index method (EIM) is applied [12]. Third, the beam propagation method (BPM) is used to study the wave propagation behavior in waveguides [13].

2.2 Transfer Matrix Method

Basically, Maxwell's equations in a source-free, homogeneous, isotropic dielectric medium for electric field and magnetic field are given as

$$\nabla \times \vec{E} = -\mu_0 \frac{\partial \vec{H}}{\partial t}, \tag{2.1}$$

$$\nabla \times \vec{H} = \epsilon_0 n^2 \frac{\partial \vec{E}}{\partial t}, \tag{2.2}$$

where ε_0 is the permittivity and μ_0 is the permeability in free space. The dielectric permittivity and the magnetic permeability are set as $\varepsilon = \varepsilon_0 n^2$ and $\mu = \mu_0$, and n is the refractive index.

The electromagnetic fields of a plane wave propagating along the z-direction with a

propagation constant β are

$$\vec{E} = \vec{E}(x,y)e^{j(\omega t - \beta z)}, \tag{2.3}$$

$$\vec{H} = \vec{H}(x,y)e^{j(\omega t - \beta z)}. \tag{2.4}$$

Since the electromagnetic fields E and H are independent of y in a planar waveguide, as shown in Figure 2-1, so we set $\partial E/\partial y = 0$ and $\partial H/\partial y = 0$, and substitute Eq. (2.3) and Eq. (2.4) into Eq. (2.1) and Eq. (2.2), then we can get two types of modes with mutually orthogonal polarization states. One is the transverse electric (TE) mode, of which the longitudinal electric field is zero ($E_z = 0$), and the other one is the transverse magnetic (TM) mode, of which the longitudinal magnetic field is zero ($H_z = 0$).

2.2.1 TE Modes of Multilayer Stack

For TE modes propagating along z-direction in a slab structure as shown in Figure 2-1, the fields include field components H_x, E_y and H_z. The relations between components of the electromagnetic fields can be resolved as

$$H_x = -\frac{\beta}{\omega\mu}E_y, \tag{2.5}$$

$$H_z = -\frac{1}{j\omega\mu}\frac{\partial E_y}{\partial x}, \tag{2.6}$$

$$E_y = -\frac{1}{j\omega\epsilon_0 n^2}\left(\frac{\partial H_z}{\partial x} + j\beta H_x\right), \tag{2.7}$$

$$E_x = E_z = H_y = 0, \tag{2.8}$$

and we define two field variables U and V as

$$U = E_y, \tag{2.9}$$

$$V = \omega\mu H_z, \tag{2.10}$$

4

which describe the TE and the TM fields distribution. Then we substitute them into Eqs. (2.5) to (2.7) and obtain the relations as

$$\frac{\partial U(x)}{\partial x} = -jV, \tag{2.11}$$

$$\frac{\partial V(x)}{\partial x} = j(\beta^2 - k^2 n^2)U, \tag{2.12}$$

where

$$k = \omega\sqrt{\mu_0 \epsilon_0}, \tag{2.13}$$

$$n^2 = \frac{\epsilon}{\epsilon_0}. \tag{2.14}$$

While Eqs. (2.11) and (2.12) are differentiated with respect to x, it can be derived as

$$\frac{\partial^2 U(x)}{\partial x^2} = (\beta^2 - k^2 n^2)U, \tag{2.15}$$

$$\frac{\partial^2 V(x)}{\partial x^2} = (\beta^2 - k^2 n^2)V, \tag{2.16}$$

then we can obtain the general solutions of Eqs. (2.15) and (2.16) as

$$U = Ae^{-j\kappa x} + Be^{+j\kappa x}, \tag{2.17}$$

$$V = j\frac{\partial U(x)}{\partial x} = \kappa(Ae^{-j\kappa x} - Be^{+j\kappa x}), \tag{2.18}$$

where κ is the transverse propagation constant and

$$\kappa^2 = k^2 n^2 - \beta^2. \tag{2.19}$$

If boundary conditions are set as $U_0 = U(0)$ and $V_0 = V(0)$ at the input plane $x = 0$, i.e.

$$U_0 = A + B, \tag{2.20}$$

$$V_0 = \kappa(A - B), \tag{2.21}$$

we can obtain

$$A = \frac{1}{2}(U_0 + \frac{V_0}{\kappa}), \qquad (2.22)$$

$$B = \frac{1}{2}(U_0 - \frac{V_0}{\kappa}). \qquad (2.23)$$

According to Eqs. (2.17) to (2.23), a simple matrix $\mathbf{M}$ relation between the output quantities U, V and the input U_0, V_0 can be concluded as

$$\begin{pmatrix} U_0 \\ V_0 \end{pmatrix} = \mathbf{M} \begin{pmatrix} U \\ V \end{pmatrix}, \qquad (2.24)$$

where $\mathbf{M}$ is the characteristic matrix,

$$\mathbf{M} = \begin{pmatrix} \cos \kappa x & (j/\kappa) \sin \kappa x \\ j\kappa \sin \kappa x & \cos \kappa x \end{pmatrix}. \qquad (2.25)$$

Next, consider a multilayer slab waveguide of r layers, as shown in Figure 2-1, and the thickness and the refractive index of ith layer are d_i and n_i, where $i = 2 \sim r-1$. The characteristic matrix $\mathbf{M}$ at the ith layer is

$$M_i = \begin{bmatrix} \cos(\kappa_i d_i) & \frac{j}{\kappa_i} \sin(\kappa_i d_i) \\ j\kappa_i \sin(\kappa_i d_i) & \cos(\kappa_i d_i) \end{bmatrix}, \qquad (2.26)$$

where

$$\kappa_i^2 = k^2 n_i^2 - \beta^2. \qquad (2.27)$$

The relation of each layer is given by

$$\begin{bmatrix} U_{i-1} \\ V_{i-1} \end{bmatrix} = M_i \begin{bmatrix} U_i \\ V_i \end{bmatrix}, \qquad (2.28)$$

the field variables of the cover and the substrate, U_r, V_r and U_1, V_1 are related by

$$\begin{bmatrix} U_1 \\ V_1 \end{bmatrix} = \mathbf{M} \begin{bmatrix} U_r \\ V_r \end{bmatrix}, \qquad (2.29)$$

6
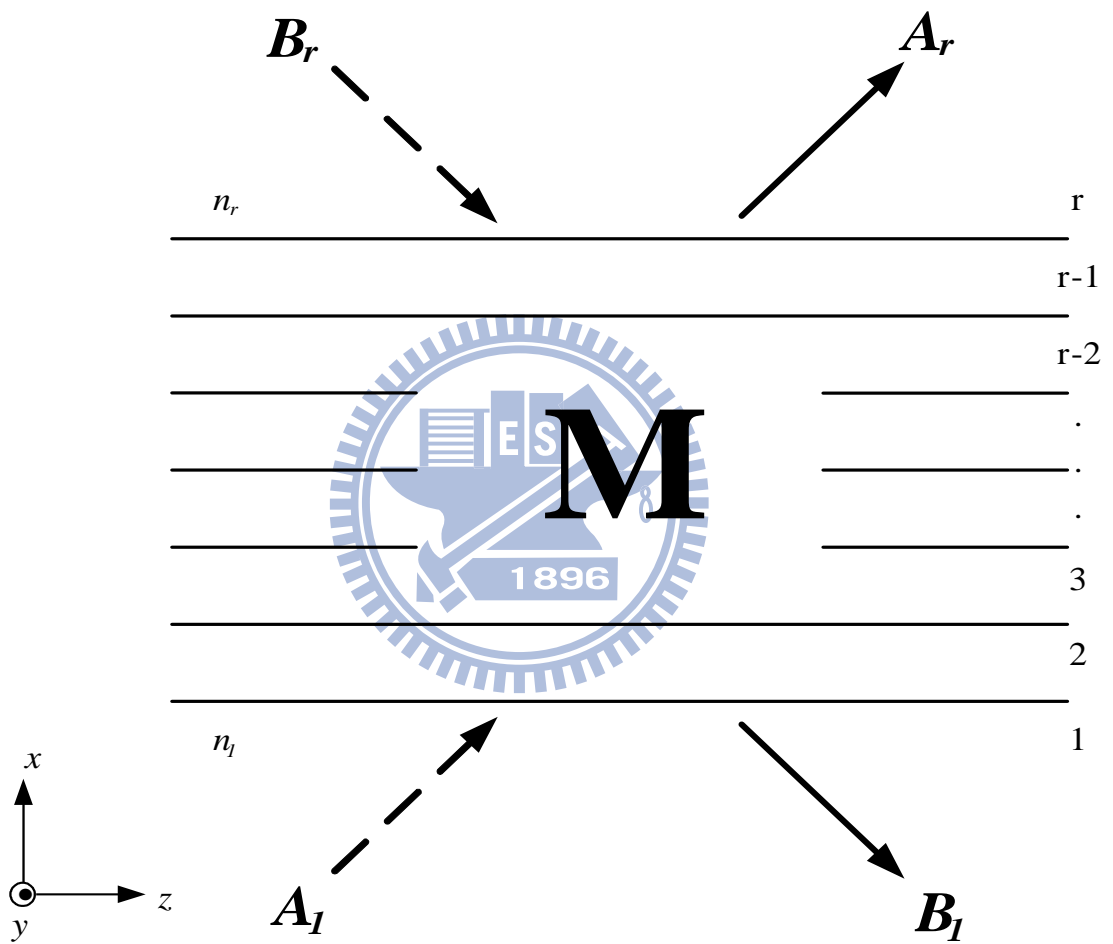
Figure 2-1: Sketch of a multilayer waveguide with the z-propagation direction.

where the product of the individual matrices is given by

$$\mathbf{M} \equiv \begin{bmatrix} m_{11} & m_{12} \\ m_{21} & m_{22} \end{bmatrix} = \prod_{i=2}^{r-1} M_i = M_2 M_3 \cdots M_{r-1}. \tag{2.30}$$

Since the modes guided in multilayer slab waveguides contain no input components from outermost layer, i.e., $A_1 = 0$ and $B_r = 0$. The field variables of the cover and the substrate are given by

$$\begin{aligned} U_1 &= B_1, \quad V_1 = -\kappa_1 B_1, \\ U_r &= A_r, \quad V_r = \kappa_r A_r, \end{aligned} \tag{2.31}$$

and by substituting Eq. (2.31) into Eq. (2.29), we can obtain the dispersion relation of multilayer slab waveguides as

$$\kappa_1(m_{11} + \kappa_r m_{12}) + (m_{21} + \kappa_r m_{22}) = 0. \tag{2.32}$$

Solving the Eq. (2.32), we can obtain the propagation constants of TE modes for a multilayer slab waveguide.

2.2.2 TM Modes of Multilayer Stack

For TM modes propagating along z-direction, it can be derived that $H_x = H_z = E_y = 0$. According to Maxwell's equations, we can obtain the relations as that we derive for TE modes as

$$E_x = \frac{\beta}{\omega \varepsilon_0 n^2} H_y, \tag{2.33}$$

$$E_z = \frac{1}{j\omega \varepsilon_0 n^2} \frac{\partial H_y}{\partial x}, \tag{2.34}$$

$$H_y = \frac{1}{j\omega \mu} (\frac{\partial E_z}{\partial x} + j\beta E_x), \tag{2.35}$$

then we can define two field variables U and V as

8

$$U = H_y, \tag{2.36}$$

$$V = \omega\varepsilon_0 E_z. \tag{2.37}$$

Substituting them into Eqs. (2.33) to (2.35), we obtain the relations as

$$\frac{\partial U}{\partial x} = -jn^2 V, \tag{2.38}$$

$$\frac{\partial V}{\partial x} = j(\frac{\beta^2}{n^2} - k^2)U. \tag{2.39}$$

While differentiating Eqs. (2.38) and (2.39) with respect to x, it can be derived as

$$\frac{\partial^2 U}{\partial x^2} = (\beta^2 - k^2 n^2)U, \tag{2.40}$$

$$\frac{\partial^2 V}{\partial x^2} = (\beta^2 - k^2 n^2)V. \tag{2.41}$$

then we can obtain the general solutions of Eqs. (2.40) and (2.41) as

$$U = Ae^{-j\kappa x} + Be^{+j\kappa x}, \tag{2.42}$$

$$V = j\frac{\partial U}{\partial x} = -\frac{\kappa}{n^2}(Ae^{-j\kappa x} - Be^{+j\kappa x}), \tag{2.43}$$

where

$$\kappa^2 = k^2 n^2 - \beta^2. \tag{2.44}$$

Similarly, we can get the transfer matrix of the TM modes as

$$M_i = \begin{bmatrix} \cos(\kappa_i d_i) & -j(\frac{n_i^2}{\kappa_i})\sin(\kappa_i d_i) \\ -j(\frac{\kappa_i}{n_i^2})\sin(\kappa_i d_i) & \cos(\kappa_i d_i) \end{bmatrix}, \tag{2.45}$$

and the dispersion relation of TM modes is then given by

$$-\frac{\kappa_1}{n_1^2}(m_{11} - \frac{\kappa_r}{n_r^2}m_{12}) + (m_{21} - \frac{\kappa_r}{n_r^2}m_{22}) = 0. \tag{2.46}$$

Solving the Eq. (2.46), we can obtain the propagation constants of TM modes for a multilayer slab waveguide.

2.3   Effective Index Method

The effective index method (EIM) was initially proposed from modifying Marcatili's method [19] for analyzing the rectangular-core dielectric waveguides [20]. The basic principle of the method is to replace the waveguide by an equivalent slab waveguide with a refractive index profile from the 3-D shape of the original waveguide. Since the method can make the analysis more efficient and simpler, it might be the most practical one of several approximate techniques.

The ridge 3-D structure is divided into 2-D waveguide with light confinement in the the y- (lateral) direction as shown in Figure 2-2. In each region, we use the transfer matrix method (TMM) to solve the effective index in the x- (vertical) direction and use the TMM again to obtain the final effective index in the y- (lateral) direction with indices distribution of $N'_{\text{eff}}/N_{\text{eff}}/N'_{\text{eff}}$.
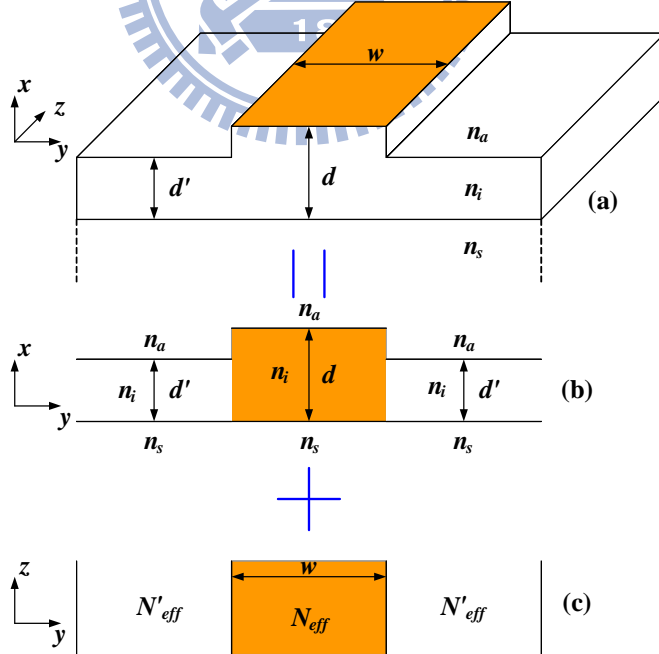
Figure 2-2: Effective Index Method: (a) 3-D ridge waveguide; (b) 2-D equivalence in the x-y plane; (c) 2-D equivalence in the z-y plane.

10

2.4 Beam Propagation Method

The beam propagation method (BPM) is used to analyze light propagation behavior in the waveguide by solving scalar wave equation along the z- (longitudinal) direction of the waveguide. BPM was derived from a paraxial form of the Helmholtz equation, known as the Fresnel equation. This method is used on waveguide structures with arbitrary cross-section geometries.

In most cases, it is regard as a optical propagation problem starting from the scalar Helmholtz equation. The 3-D scalar wave equation is given by

$$\frac{\partial^2 E}{\partial x^2} + \frac{\partial^2 E}{\partial y^2} + \frac{\partial^2 E}{\partial z^2} + k^2 n^2(x, y, z)E = 0, \tag{2.47}$$

where E is the electric field, k is the wave number, and n is the refractive index in the domain of interest.

If the field $E = \psi(x, y, z)\exp(-jk_0 n_0 z)$, where ψ is an axially slowly varying function, n_0 is the mean refractive index of the medium, and z is the propagation direction. For a light beam confined in a 2-D cross-sectional waveguide with an index profile $n(x, z)$ and paraxial propagating along the z-direction, the scalar wave equation can be modified as

$$\frac{\partial^2 \Psi}{\partial x^2} + \frac{\partial^2 \Psi}{\partial z^2} + k_0^2 n^2(x, z)\Psi = 0, \tag{2.48}$$

assume $\Psi = \psi(x, z)\exp(-jk_0 n_0 z)$ is a wave propagating mainly in the z-direction.

With the slowly varying envelope approximation [15], [16], Eq. (2.48) can be resolved as

$$2jkn_0 \frac{\partial \psi}{\partial z} = \frac{\partial^2}{\partial x^2}\psi + k^2 \left[n^2(x, z) - n_0^2\right]\psi, \tag{2.49}$$

then we use a uniform discretization step sizes $\triangle x$ and $\triangle z$, we can derive as

$$2jk_0 n_0 \frac{\partial \psi_i}{\partial z} = \frac{\psi_{i+1} + \psi_{i-1} - 2\psi_i}{(\triangle x)^2} + k^2 \left[n^2(x, z) - n_0^2\right]\psi_i, \tag{2.50}$$

where ψ_i is the field at $(u\triangle x, z)$ and $\triangle x$ denotes the discretization step in the x-direction. We can repeat these process until the wave reaches the boundary of the domain resulting in final field distribution. The finite difference BPM (FDBPM) is more accurate than conventional fast Fourier transform (FFTBPM) in high index contrasts.

There is another method, a linear combination of the "forward-diffrence" method and the "backward-diffrence" method, called Crank-Nicolson scheme. By applying the Crank-Nicolson scheme, we obtain

$$\psi_{i-1}^{v+1} + a_i^+ \psi_i^{v+1} + \psi_{i+1}^{v+1} = -\psi_{i-1}^{v} - a_i^- \psi_i^{v} - \psi_{i+1}^{v}, \tag{2.51}$$

where

$$a_i^+ = -2 + k_0^2(n_i^2 - n_0^2)(\triangle x)^2 - 4jk_0n_0(\triangle x)^2/\triangle z. \tag{2.52}$$

$$a_i^- = -2 + k_0^2(n_i^2 - n_0^2)(\triangle x)^2 + 4jk_0n_0(\triangle x)^2/\triangle z. \tag{2.53}$$

the superscripts and subscripts in Eq. (2.51) denote the z- and x-coordinates, respectively. For example, ψ_i^v is the slowly-varying field at $(i \cdot \Delta x, v \cdot \Delta z)$.

The transparent boundary condition (TBC) [21] is used to deal with the radiation reflected back from the computation boundaries. For waveguide structures whose refractive indices differ greatly from the average refractive index (the reference index), the Padé approximent operator [22] is also implemented in the simulation.

For this research, we utlize the BeamPROP software included in the commerical software package R-soft V.5.1 to simulate the optical propagation characteristics of our designed devices.

Chapter 3

Design of Si-Based Dual ARROW Power Splitters

3.1 Introduction

ARROW structure was first reported in 1986, which utilizes the Fabry-Pérot reflection instead of the total internal reflection (TIR) as the guiding mechanism. In contrast to the conventional waveguides, the ARROW structures are promising for photonic integrated circuits (PICs) due to their distinctive features: (a) effective single-mode propagation, (b) low loss of effective single mode, (c) large core size suitable for efficient connection to fibers, (d) selective losses depending on the wavelength and on the polarization of the light, (e) large fabrication tolerance for refractive indices and thicknesses of cladding layers between the core and the substrate, and (f) various choice of waveguide materials for each layer [23].

3.2 Characteristics of an ARROW Structure

The basic configuration of a slab ARROW waveguide $(n_\mathrm{a}/n_\mathrm{g}/n_\mathrm{h}/n_\mathrm{l}/n_\mathrm{s})$ is shown in Figure 3-1. For an ARROW structure, light is confined by antiresonance conditions within the cladding layers and by total internal reflection at the air–core interface. The refractive index of the first cladding layer is higher than the core and the second cladding layers, as shown in Figures 3-1 and 3-2. The amount of power passing through the interface corresponds to the propagation loss.

13

In order to achieve high reflectivity at the core-cladding interface, both of the first and the second cladding thicknesses are designed to satisfy the antiresonance condition to produce the destructive interference within them, which is known as Fabry-Pérot resonance [24]. The reflection from the interference within the cladding layers depends strongly upon the polarization of guided light, which is a kind of multiple Fresnel reflection.
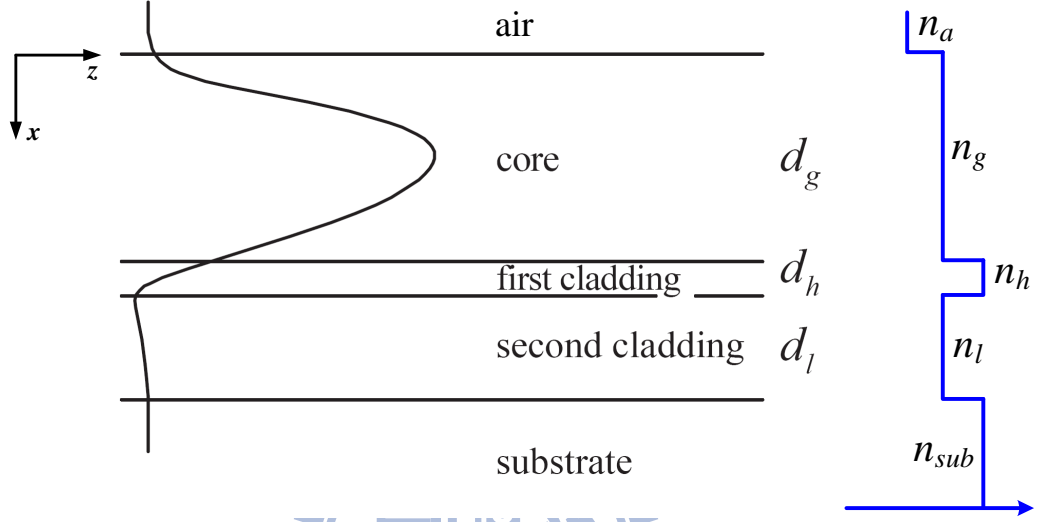
Figure 3-1: The cross-section schematic of a slab ARROW waveguide.

In this following, we derive the confinement condition of the planar ARROW structure from the ray–optical picture, as shown in Figure 3-2. Supposing that a zig-zag beam with a certain incident angle is guided in the core region. The optical field decays evanescently in the air region because of the total internal reflection at the air-core interface. The transverse propagation constant κ_{g} in the core region and κ_{a} in the air region are given by

$$\kappa_{\mathrm{g}} = \sqrt{k_0^2 n_{\mathrm{g}}^2 - \beta^2}, \tag{3.1}$$

$$\kappa_{\mathrm{a}} = -j\gamma_{\mathrm{a}}, \tag{3.2}$$

$$\gamma_{\mathrm{a}} \equiv \sqrt{\beta^2 - k_0^2 n_{\mathrm{a}}^2}, \tag{3.3}$$

where $k_0 n_{\mathrm{g}} > \beta > k_0 n_{\mathrm{a}}$, and β is the propagation constant.

14
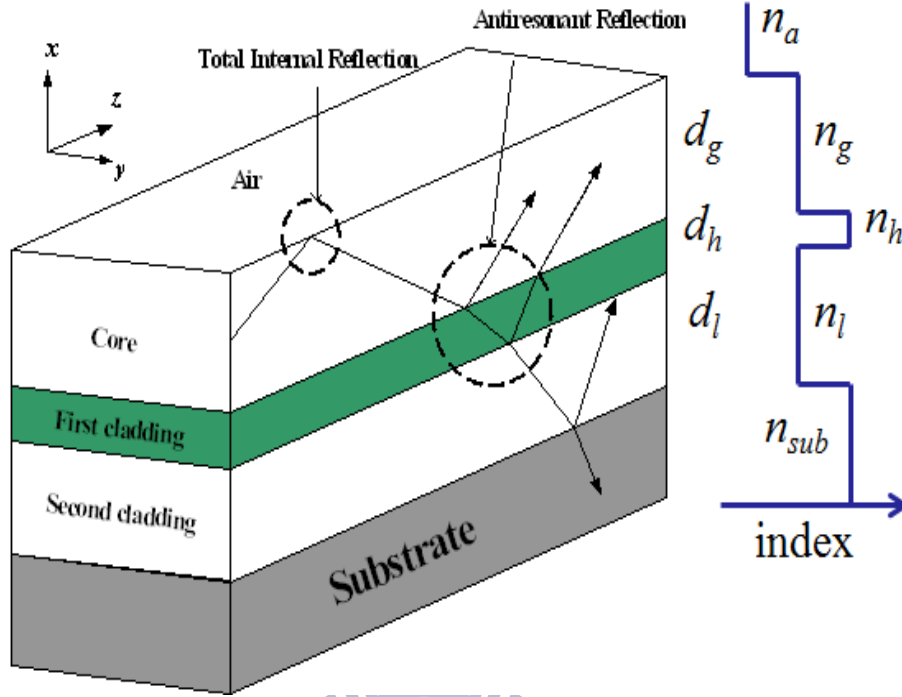
Figure 3-2: Light propagation behavior and the refractive indices of the core and the cladding layers in a ARROW structure.

For TE mode, the reflection coefficient r_{ga} at the air–core interface is given by

$$r_{\mathrm{ga}} = \frac{\kappa_{\mathrm{g}} - \kappa_{\mathrm{a}}}{\kappa_{\mathrm{g}} + \kappa_{\mathrm{a}}} = \frac{\kappa_{\mathrm{g}} + j\gamma_{\mathrm{a}}}{\kappa_{\mathrm{g}} - j\gamma_{\mathrm{a}}} \equiv |r_{\mathrm{ga}}| \exp(j\phi_{\mathrm{ga}}), \tag{3.4}$$

where ϕ_{ga} is the phase-shift of the reflected wave. If the core size is large, i.e., $\gamma_{\mathrm{a}} \gg \kappa_{\mathrm{g}}$, then ϕ_{ga} approaches π. The reflection coefficient r_{gh} at the interface of the core and the first cladding is given by

$$r_{\mathrm{gh}} = \frac{\kappa_{\mathrm{g}} - \kappa_{\mathrm{h}}}{\kappa_{\mathrm{g}} + \kappa_{\mathrm{h}}} \equiv |r_{\mathrm{gh}}| \exp(j\phi_{\mathrm{gh}}), \tag{3.5}$$

where $\kappa_{\mathrm{h}} \gg \kappa_{\mathrm{g}}$, so ϕ_{gh} approaches π.

In order to form a constructive interference in the core layer, the following condition should be satisfied

$$-2\kappa_{\mathrm{g}}d_{\mathrm{g}} + \phi_{\mathrm{ga}} + \phi_{\mathrm{gh}} = 0 \Rightarrow \kappa_{\mathrm{g}}d_{\mathrm{g}} \approx \pi, \tag{3.6}$$

15

if the core size is not large enough, Eq. (3.6) must be modified as

$$2\kappa_{\mathrm{g}}d_{\mathrm{ge}} = 2\pi \Rightarrow \kappa_{\mathrm{g}}d_{\mathrm{ge}} = \pi, \tag{3.7}$$

where d_{ge} is the effective thickness of the core layer.

Rearranging Eq. (3.6) and applying Snell's law, we can derive Eq. (3.8) as

$$\frac{2\pi}{\lambda_0}n_{\mathrm{g}}\cos\theta_{\mathrm{g}}d_{\mathrm{g}} \approx \pi, \tag{3.8}$$

$$\Rightarrow \cos\theta_{\mathrm{h}} = \left(1 - \sin^2\theta_{\mathrm{h}}\right)^{\frac{1}{2}} = \left(1 - \frac{n_{\mathrm{g}}^2}{n_{\mathrm{h}}^2}\sin^2\theta_{\mathrm{g}}\right)^{\frac{1}{2}}, \tag{3.9}$$

$$\approx \left(1 - \frac{n_{\mathrm{g}}^2}{n_{\mathrm{h}}^2} + \frac{\lambda_0^2}{4n_{\mathrm{h}}^2 d_{\mathrm{g}}^2}\right)^{\frac{1}{2}}, \tag{3.10}$$

where θ_{g} and θ_{h} respectively represent the ray angle in the core layer and the first cladding layer. From the transmission characteristics of a Fabry-Pérot resonator, high reflection of cladding layer exists under the antiresonance condition. The antiresonance condition is defined as

$$2\kappa_i d_i = (2m+1)\pi, \qquad m = 0, 1, 2, \cdots \tag{3.11}$$

where κ_i represents the transverse propagation constant in the i cladding layer.

From Eqs. (3.10) and (3.11), the antiresonance conditions of the first and the second cladding layers are derived as

$$d_{\mathrm{h}} = \frac{\lambda_0}{4n_{\mathrm{h}}}\left(1 - \frac{n_{\mathrm{g}}^2}{n_{\mathrm{h}}^2} + \frac{\lambda_0^2}{4n_{\mathrm{h}}^2 d_{\mathrm{g}}^2}\right)^{-\frac{1}{2}}(2P+1), \qquad P = 0, 1, 2, \cdots \tag{3.12}$$

$$d_{\mathrm{l}} = \frac{\lambda_0}{4n_{\mathrm{l}}}\left(1 - \frac{n_{\mathrm{g}}^2}{n_{\mathrm{l}}^2} + \frac{\lambda_0^2}{4n_{\mathrm{l}}^2 d_{\mathrm{g}}^2}\right)^{-\frac{1}{2}}(2Q+1). \qquad Q = 0, 1, 2, \cdots \tag{3.13}$$

If the refractive index of the second cladding layer n_{l} and the core layer n_{g} are the same, Eq. (3.13) can be simplified as

$$d_{\mathrm{l}} \approx \frac{d_{\mathrm{g}}}{2}(2Q+1). \tag{3.14}$$

3.3 Design of the Slab ARROW Structure

For single-mode propagation, the core size of the ARROW structure can be large to get better coupling efficiency with the single-mode fiber. In our slab ARROW structure, the refractive indices of the core layer n_g, the first cladding layer n_h, and the second cladding layer n_l are chosen as 1.45, 3.7, and 1.45, respectively. In order to perform the series of simulations in the following sections, all layer's material parameters of the slab ARROW structure need to be defined. In the slab ARROW structure, we chose silicon dioxide (SiOx) as the core material and its thickness was designed as 2.0 μm. From Eqs. (3.12) and (3.13), we chose $P = 0$ and $Q = 0$ for minimum the thicknesses of the first and the second cladding layers. Amorphous silicon was chosen as the material of the first cladding layer and its thickness was designed as 0.12 μm. For fabrication convenience, we chose the same material of the second cladding layer as the core layer, and its thickness must be designed as 1.0 μm. The parameters of the slab waveguide are shown in Table 3.1, and the operation wavelength λ is 1.55 μm. Table 3.2 shows the propagation losses of first three modes of both TE and TM polarizations.

For reducing the propagation loss of the fundamental mode, we used two antiresonant cavities under the core layer, as shown in Figure 3-3 and Table 3.1. Our fabrication process was chosen (100) p-type silicon as the substrate.

The loss is defined as

$$
\begin{aligned}
\text{Loss (dB/cm)} &= -10 \log_{10} \frac{P_{\text{out}}}{P_{\text{in}}}, && (3.15) \\
&= -10 \log_{10} \frac{\left[(\mathrm{E}_0 \cdot e^{-j\beta \cdot (1 \text{ cm})})(\mathrm{E}_0 \cdot e^{-j\beta \cdot (1 \text{ cm})})^* \right]}{\mathrm{E}_0 \mathrm{E}_0{}^*}, \\
&= -10 \log_{10} e^{2 k_0 \text{Im}\{N_{\text{eff}}\}(1 \text{ cm})}, \\
&= -20 \cdot k_0 \text{Im}\{N_{\text{eff}}\}(1 \text{ cm}) \cdot \log_{10} e, && (3.16)
\end{aligned}
$$

where

$$
\beta = k_0 N_{\text{eff}} = k_0 (\text{Re}\{N_{\text{eff}}\} + \text{Im}\{N_{\text{eff}}\}) = \frac{2\pi}{\lambda} (\text{Re}\{N_{\text{eff}}\} + \text{Im}\{N_{\text{eff}}\}), \qquad (3.17)
$$

β is the propagation constant, k_0 is the wave number, and N_{eff} is the effective index of the propagation mode in complex form.
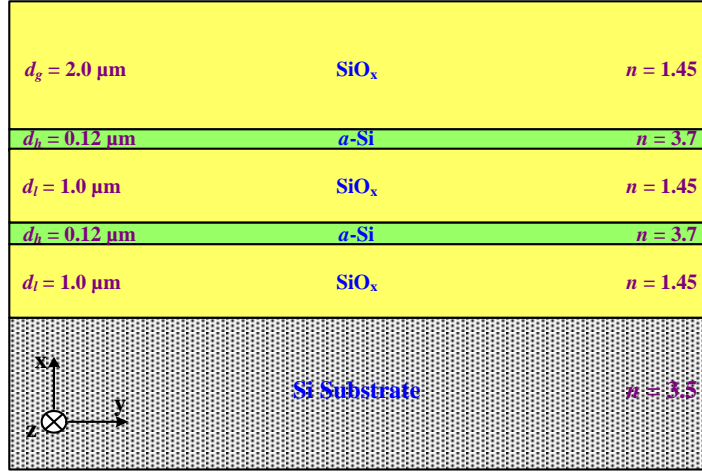
Figure 3-3: The cross-section schematic of the slab ARROW structure.

The simulation characteristics of our slab ARROW waveguide are shown in Figures 3-4 and 3-5. In Figure 3-4, when the thickness d_g of the core layer reaches about 1.5 μm, the propagation loss of the fundamental mode, TE_0, would be less than 1 dB/cm. Therefore, we chose the thickness d_g of the core layer as 2.0 μm still in the tolerance range. In Figure 3-5, when the thickness d_h of the first cladding layer reaches 0.12 μm, the propagation loss of the fundamental TE mode would be less than 1 dB/cm. Furthermore, the propagation loss within the flat region does not vary much, so it can be seen that this design has a feature of large tolerance.

Figures 3-6(a) and (b) show the field profiles of the fundamental TE mode (E-field along y-direction) when using one cavity and two cavities. The oscillation behavior of the extension tail of the field profile in the high index structure in Figure 3-6(b) is less than that in Figure 3-6(a), which means that the loss is reduced when using two antiresonant cavities. Figures 3-6(c) and (d) show the field profiles of the fundamental TM mode (H-field along y-direction) when using one cavity and two cavities. The oscillation behavior of the extension tail of the field profile in the high index structure in Figure 3-6(d) is less than that in Figure 3-6(c), where means that the loss is reduced when using two antiresonant cavities.
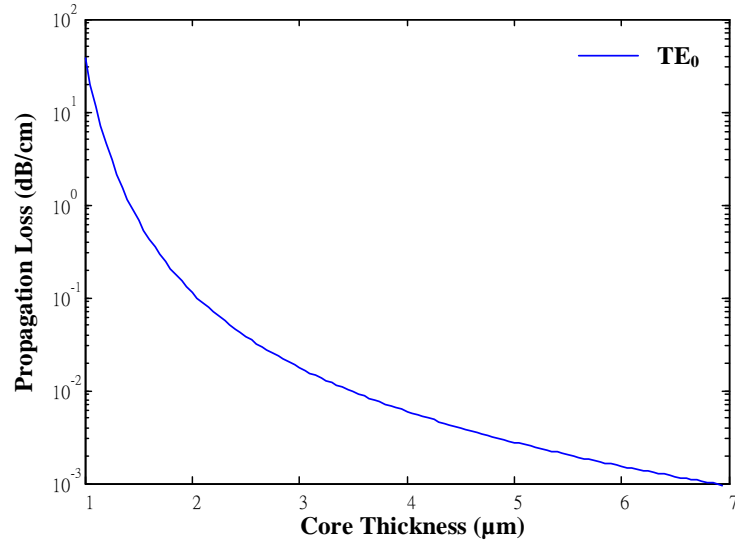
Figure 3-4: The propagation losses of the fundamental TE mode versus the core layer thickness d_{g} for the slab ARROW structure with simulation parameter values $n_{\mathrm{a}}/n_{\mathrm{g}}/n_{\mathrm{h}}/n_{\mathrm{l}}/n_{\mathrm{h}}/n_{\mathrm{l}}/n_{\mathrm{s}} = 1.0/1.45/3.7/1.45/3.7/1.45/3.5$, $d_{\mathrm{h}}/d_{\mathrm{l}}/d_{\mathrm{h}}/d_{\mathrm{l}} = 0.12/1.0/0.12/1.0$ μm and $\lambda = 1.55$ μm.
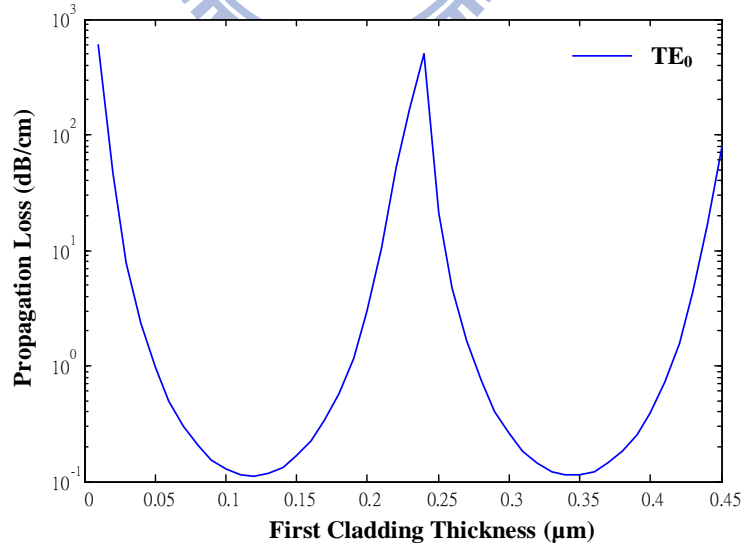
Figure 3-5: The propagation losses of the fundamental TE mode versus the first cladding layer thickness d_{h} for the slab ARROW structure with simulation parameter values $n_{\mathrm{a}}/n_{\mathrm{g}}/n_{\mathrm{h}}/n_{\mathrm{l}}/n_{\mathrm{h}}/n_{\mathrm{l}}/n_{\mathrm{s}} = 1.0/1.45/3.7/1.45/3.7/1.45/3.5$, $d_{\mathrm{g}}/d_{\mathrm{l}}/d_{\mathrm{h}}/d_{\mathrm{l}} = 2.0/1.0/0.12/1.0$ μm and $\lambda = 1.55$ μm.
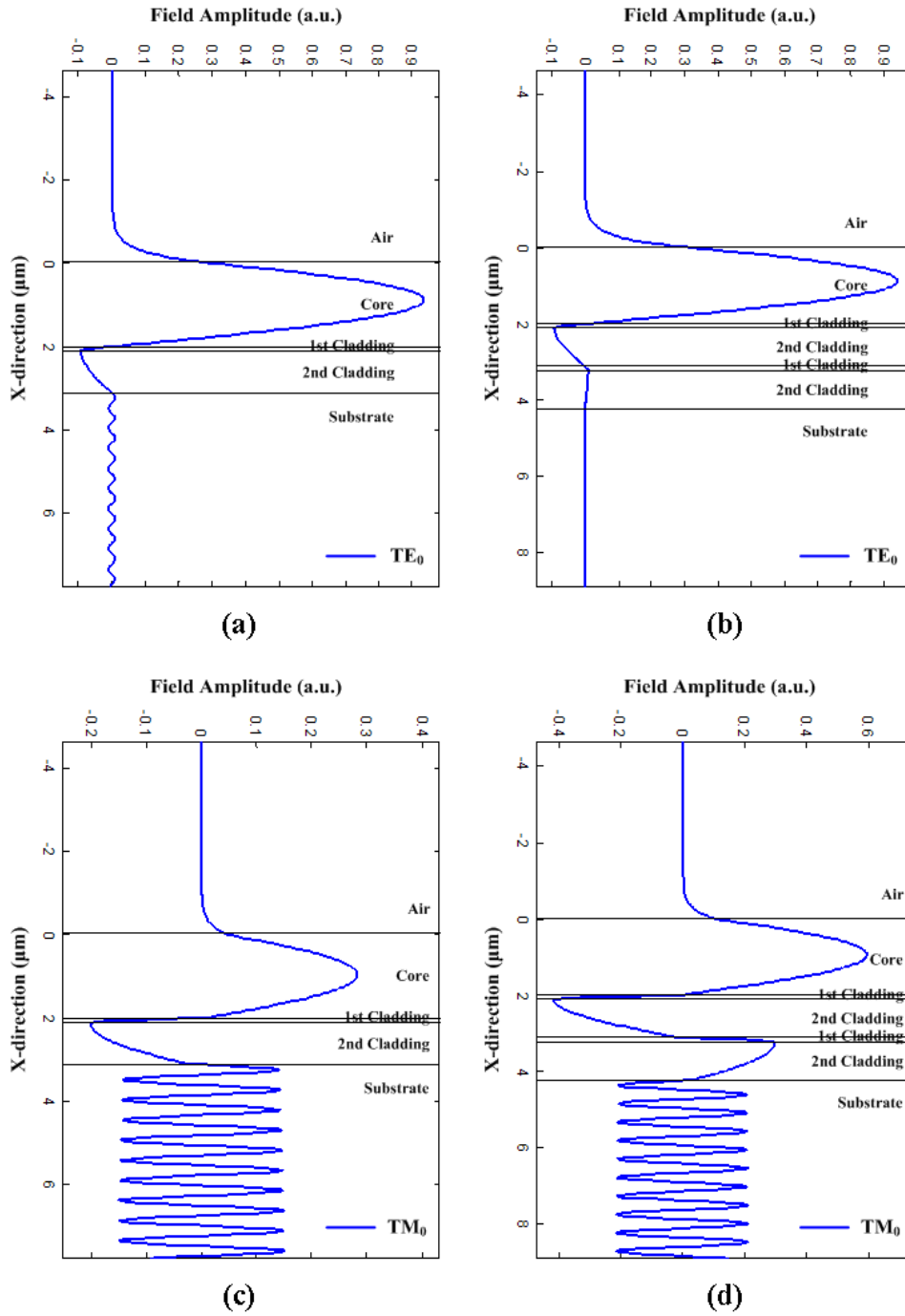
Figure 3-6: The field profiles of the fundamental TE mode: (a) one antiresonant cavity (b) two antiresonant cavities. The field profiles of the fundamental TM mode: (c) one antiresonant cavity, (d) two antiresonant cavities. The parameters are given in Table 3.1.

Table 3.1: The parameters of the slab ARROW structure at the operation wavelength λ of 1.55 μm.

	Material	Refractive Index	Thickness
Superstrate	Air	$n_a = 1.0$	
Core Layer	SiOx	$n_g = 1.45$	$d_g = 2.0~\mu$m
1st Cladding Layer	a-Si	$n_h = 3.7$	$d_h = 0.12~\mu$m
2nd Cladding Layer	SiOx	$n_l = 1.45$	$d_l = 1.0~\mu$m
1st Cladding Layer	a-Si	$n_h = 3.7$	$d_h = 0.12~\mu$m
2nd Cladding Layer	SiOx	$n_l = 1.45$	$d_l = 1.0~\mu$m
Substrate	Silicon	$n_s = 3.5$	

Table 3.2: The propagation losses of first three TE and TM modes when using only one cavity and two cavities. The unit of propagation loss is dB/cm.

	TE_0	TE_1	TE_2	TM_0	TM_1	TM_2
One Cavity	10.7	821	994	2832	12128	26404
Two Cavities	0.11	243	122	1341	8983	16873

3.4 Coupling Behavior of Dual ARROW Structures

Coupling behavior of dual ARROW structures was first investigated by Baba *et al.* for using as an uncoupled stacking, and followed by Mann *et al.* in applying the structure as a directional coupler [1]–[5]. It can be found that we can control the structural symmetry to operate a dual ARROW as a directional coupler or as two decoupled waveguides. Most of the results are accurate only in weakly coupling situations. For dual ARROW structures with leaky modes, the strong coupling between two waveguides must be considered [24]. The following is a review of the method based on the interference of the fundamental even and odd modes [25] and used to analyze the coupling efficiency of a dual ARROW structure, as shown in Figure 3-7.

The field distributed in a dual ARROW guided system can be expressed as

$$E(x, z) = A_e E_e(x) \exp(-jk_0 N_e z) + A_o E_o(x) \exp(-jk_0 N_o z), \quad (3.18)$$

$$H(x, z) = A_e H_e(x) \exp(-jk_0 N_e z) + A_o H_o(x) \exp(-jk_0 N_o z), \quad (3.19)$$

where A_e and A_o are the amplitudes of the normalized even and odd modes with effective indices N_e and N_o, respectively. Both E_e (H_e) and E_o (H_o) are the normalized electric

Superstrate

2 nd Cladding Layer

1 st Cladding Layer

Upper Core

1 st Cladding Layer

Separation Layer

1 st Cladding Layer

Lower Core

1 st Cladding Layer

2 nd Cladding Layer

x

Si Substrate

z
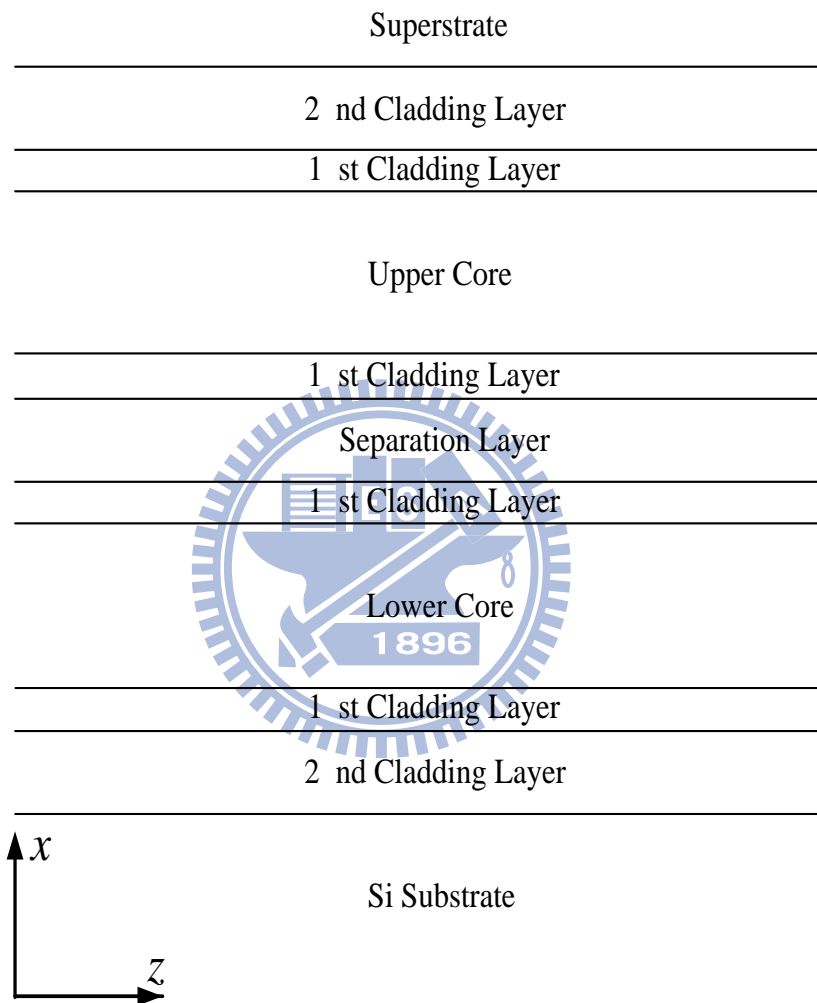
Figure 3-7: The cross-section schematic of a dual slab ARROW structure.

(magnetic) fields of even and odd modes, respectively. For TE modes, the power density S_z is

$$
\begin{aligned}
S_z(x,z) &= \frac{1}{2}\text{Re}[(\vec{E} \times \vec{H}^*) \cdot \hat{a}_z] \\
&= \frac{1}{2}\text{Re}[E_y(x,z)H_x^*(x,z)] \\
&= \frac{1}{2}\text{Re}\{A_e^2 E_e(x)H_e^*(x) + A_o^2 E_o(x)H_o^*(x) \\
&\quad + A_e A_o \cdot [E_e(x)H_o^*(x) + E_o(x)H_e^*(x)] \cdot \cos[k_0(N_e - N_o)z]\}. \quad (3.20)
\end{aligned}
$$

The even and odd modes are orthonormal with respect to the Poynting power as

$$
\begin{aligned}
P &= \int_{-\infty}^{\infty} S_z(x,z)dx = P_{g_1} + P_{g_2} + P_{else} \\
&= (A_e^2 + A_o^2) = 1, \quad (3.21)
\end{aligned}
$$

where

$$
P_{g_1}(z) = \int_{g_1} S_z(x,z)dx, \ \ P_{g_2}(z) = \int_{g_2} S_z(x,z)dx, \ \text{and} \ P_{else}(z) = \int_{else} S_z(x,z)dx, \quad (3.22)
$$

P_{g_1} is the guided power in the upper core g_1, P_{g_2} is the guided power in the lower core g_2, and P_{else} represents the remaining power in the region outside cores g_1 and g_2. Light is launched into the upper core in Figure 3-7 at the reference plane $z = 0$ such that there is a reference power P_{g_1} guided in the upper core.

To calculate the coupling efficiency $C(z)$ from the upper core in our structure to the lower core at any z position, we must investigate the power variation ΔP_{g_2} in the lower core. The power in the core g_1 at a position z is

$$
P_{g_1}(z) = A_e^2 \xi_{ee} + A_o^2 \xi_{oo} + A_e A_o(\xi_{eo} + \xi_{oe}) \cos[k_0(N_e - N_o)z], \quad (3.23)
$$

where

$$
\xi_{ij} = \frac{1}{2} \int_{g_1} E_j(x)H_i^*(x)dx, \ \ (i,j = e, o). \quad (3.24)
$$

To minimize the uncoupled power $P_{g_2}(0) + P_{else}(0)$, the cross product $A_e A_o$ is released as

$$
A_e A_o = \frac{\xi_{eo} + \xi_{oe}}{[(\xi_{ee} - \xi_{oo})^2 + (\xi_{eo} + \xi_{oe})^2]^{\frac{1}{2}}}. \quad (3.25)
$$

Assume that the power is mainly guided inside g_1 and g_2, then

$$\Delta P_{\text{else}}(z) \ll \Delta P_{g_2}(z), \tag{3.26}$$

and we can utilize the following approximations:

$$\begin{aligned}
\Delta P_{g_2}(z) &\approx -\Delta P_{g_1}(z) = P_{g_1}(0) - P_{g_1}(z) \\
&= 2A_e A_o (\xi_{\text{eo}} + \xi_{\text{oe}}) \sin^2\left[\frac{k_0(N_e - N_o)}{2}z\right].
\end{aligned} \tag{3.27}$$

We can obtain the coupling efficiency based on above equations as

$$C(z) = \frac{\Delta P_{g_2}(z)}{P_{g_1}(0)} = C_o \sin^2(\beta_c z), \tag{3.28}$$

where

$$C_o = \frac{2(\xi_{\text{eo}} + \xi_{\text{oe}})^2}{(\xi_{\text{ee}} + \xi_{\text{oo}})\left[(\xi_{\text{ee}} - \xi_{\text{oo}})^2 + (\xi_{\text{eo}} + \xi_{\text{oe}})^2\right]^{\frac{1}{2}} + (\xi_{\text{ee}} - \xi_{\text{oo}})^2 + (\xi_{\text{eo}} + \xi_{\text{oe}})^2}, \tag{3.29}$$

$$\beta_c = \frac{k_0(N_e - N_o)}{2}, \tag{3.30}$$

C_o is the maximum coupling efficiency at a length z equal to the coupling length (L_c). In the case that light is launched into the lower core, the above formulas will also be satisfied if P_{g_1} and P_{g_2} are exchanged with each other.

The size is one of the most important factors in the cost and integration capability for an integrated optical device and a compact device is always attractive, it is desirable to shorten the coupling length and in turn the device length for a coupler. We design our devices based on the theory.

3.5   Design of the Dual ARROW Power Splitters

The dual ARROW power splitter include three parts: the input region, the coupling region, and the decoupling region. The basic structure and the corresponding effective-index profile obtained by the transfer matrix method (TMM) and the effective index method (EIM) are depicted in Figures 3-8 to 3-9. Along the vertical direction, the structure was chosen as the ARROW structure instead of the conventional structure, and

we used the SiOx as the core material. It can guide lightwaves in a low-index ($n_\mathrm{g} = 1.45$) core with a large core size ($d_\mathrm{g} = 2.0\ \mu$m), and their core index and size can be compatible with a single-mode fiber, which can provide efficient coupling. Moreover, we used the a-Si as the first cladding material, because it is commonly used in semiconductor processing and the refractive index is more larger than SiOx, which can minimize the thickness of first cladding. Along the lateral direction, some regions in the y-direction were etched to make the structure be the ARROW type to confine light in the core, respectively. ARROW-based structure can be remotely coupled because of their nondecaying field profile inside the intermediate cladding layers. We can use this distinctive features to design our devices.

The width $w_{\mathrm{l}1}$ of the second cladding layer of our dual ARROW structure in the y-direction was designed as 3.5 μm based on the antiresonance conditions. The propagation loss of the fundamental mode, TM$_0$ (E-field along y-direction), would be less than 1 dB/cm. The width $w_{\mathrm{h}1}$ of the first cladding layer was calculated as 1.24 μm. For fabrication convenience and the guided efficiency enhancement, the depth d_x was chosen as 2.0 μm. The real part of N_{effH} was solved as 1.438 for TE polarization and 1.436 for TM polarization by using the Matlab programs, and the real part of N_{effL} was 1.408 for TE polarization and 1.403 for TM polarization. The effective indices of the dual ARROW structure are shown in Table 3.3.

The parameters of the dual ARROW structure are shown in Table 3.4. The propagation losses of one cavity to fifteen cavities are shown in Table 3.5, and Figure 3-10 shows the relations between the propagation losses of the fundamental TM mode and the number of cavities.

A dual ARROW structure can operate as a directional coupler or as two decoupled waveguides by controlling the structural symmetry. In order to simplify the structure of our dual ARROW waveguides, we designed the input region as the decoupling region. In the decoupling region, we chose $w_{\mathrm{h}2}$ and $w_{\mathrm{l}2}$ as 0.5 and 4.24 μm to reduce the coupling efficiency by satisfying the antiresonance conditions. In the coupling region, we chose $w_{\mathrm{h}3}$ and $w_{\mathrm{l}3}$ as 0.5 and 19.2 μm to enhance the coupling efficiency by satisfying the resonance conditions. From these simulation results, we used twelve cavities to reduce the propagation loss in the lateral direction.
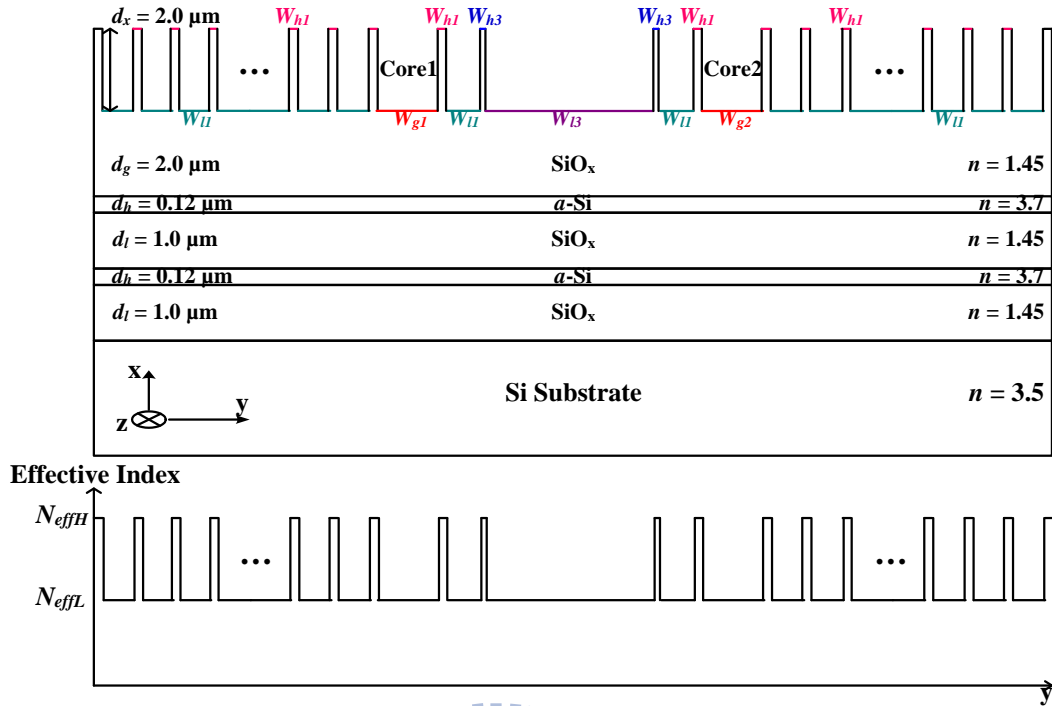
Figure 3-8: The cross-section schematic and the corresponding effective-index profile in the coupling region of the dual ARROW structure.
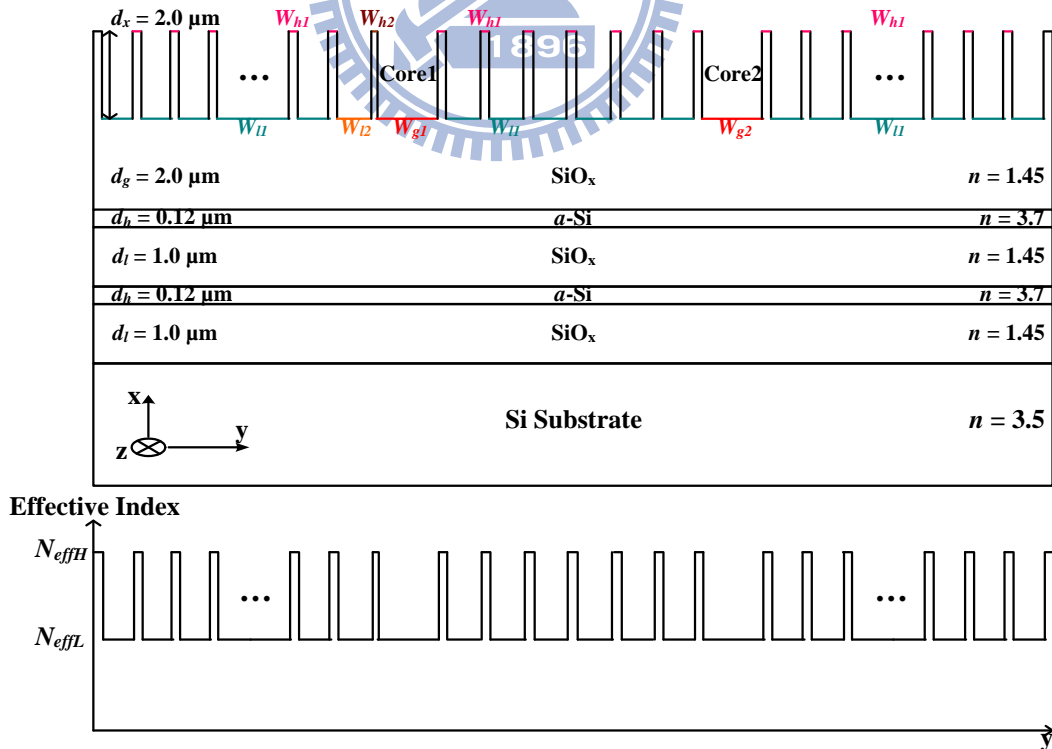
Figure 3-9: The cross-section schematic and the corresponding effective-index profile in the decoupling region of the dual ARROW structure.

Table 3.3: The effective indices of the dual ARROW structure at the operation wavelength λ of 1.55 μm.

	TE$_0$	TM$_0$
N_{effH}	1.438 - 1.69 $\times$ 10^{-8} i	1.436 - 2.46 $\times$ 10^{-4} i
N_{effL}	1.408 - 3.21 $\times$ 10^{-7} i	1.403 - 3.81 $\times$ 10^{-3} i

Table 3.4: The parameters of the dual ARROW power splitters at the operation wavelength λ of 1.55 μm.

n_{g}	1.45	n_{h}	3.7	n_{l}	1.45	n_{s}	1.35
d_{g} (μm)	2.0	d_{h} (μm)	0.12	d_{l} (μm)	1.0	d_{x} (μm)	2.0
w_{g1}, w_{g2} (μm)			7.0	w_{h1} (μm)	1.24	w_{l1} (μm)	3.5
w_{h2} (μm)	0.5	w_{l2} (μm)	4.24	w_{h3} (μm)	0.5	w_{l3} (μm)	19.2

3.6 Simulation Results for the Dual ARROW Power Splitters

Figure 3-11 shows the two-dimensional field profiles of even and odd modes (E-field along y-direction) in the dual ARROW structure for two cores with twelve cavities for TM polarization when the separation width is 30 μm in the decoupling region, and the propagation loss is 0.11 dB/cm. Figure 3-12 shows the two-dimensional field profiles of even and odd modes in the dual ARROW structure for TM polarization when the separation width is 30 μm in the coupling region. In the coupling region, our designed ARROW structure can be remotely coupled because of their nondecaying field profile inside the intermediate cladding. The propagation losses of the first ten modes of TM polarization in the decoupling region and the coupling region are shown in Tables 3.6 and 3.7, respectively. For the dual ARROW structure, when the beam is launched into

Table 3.5: The relations between the propagation losses of the fundamental TM mode and the number of cavities. The unit of prapagation loss is dB/cm.

Number of Cavities	1	2	3	4	5	6	7	8
Propagation Loss	82.9	11.0	1.57	0.31	0.14	0.12	0.11	0.11
Number of Cavities	9	10	11	12	13	14	15	
Propagation Loss	0.11	0.11	0.10	0.10	0.10	0.10	0.10	
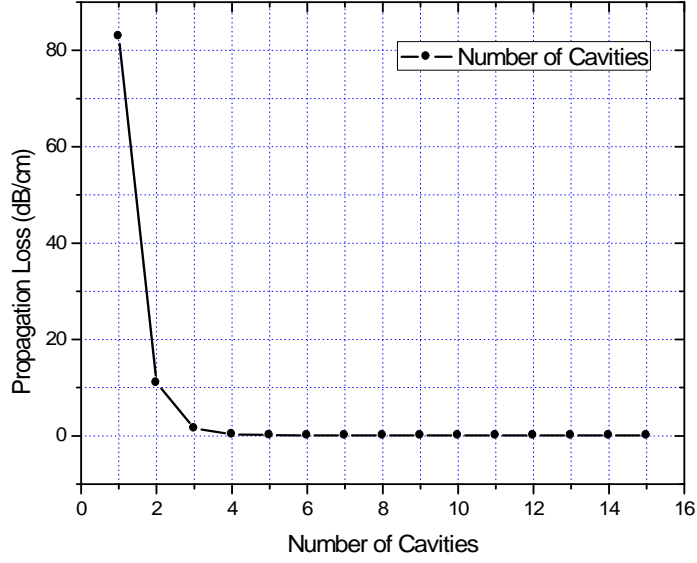
Figure 3-10: The relations between the propagation losses of the fundamental TM mode and the number of cavities.

either core, only two modes, TM_0 and TM_1, are dominantly excited. So the coupling theory in Section 3.4 can be used to design the power splitters.

The coupling length can be obtained by

$$L_c = \frac{\lambda}{2(N_{ei} - N_{oi})},$$ (3.31)

when only TM_0 and TM_1 modes are dominant, where λ is the operation wavelength and N_{ei}, N_{oi} ($i = E$ or M for TE polarization or TM polarization) are the real part of effective indices of even and odd modes, respectively.

The calculated coupling length is 4300 μm and the separation width is 30 μm. In our research, we designed the length of the coupling region at $z = L_c$ / 2 to equally split the power of incoming signals into two output ports with an equal power. When the beam is launched into the left core and the right core, the beam propagation method (BPM) simulation results are shown in Figures 3-13 and 3-14. The coupling length is almost the same as the value calculated by using the Matlab programs.

The total length of the dual ARROW power splitter was designed as 14000 μm with 4000-μm, 2150-μm ($L_c/2$), and 7850-μm lengths of the input region, the coupling region,

28
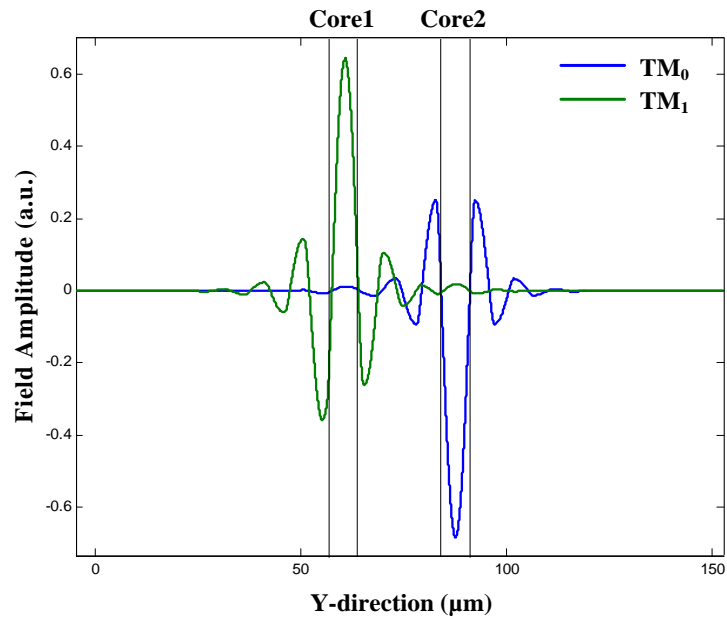
Figure 3-11: The two-dimensional field profiles of even and odd modes for TM polarization in the decoupling region.
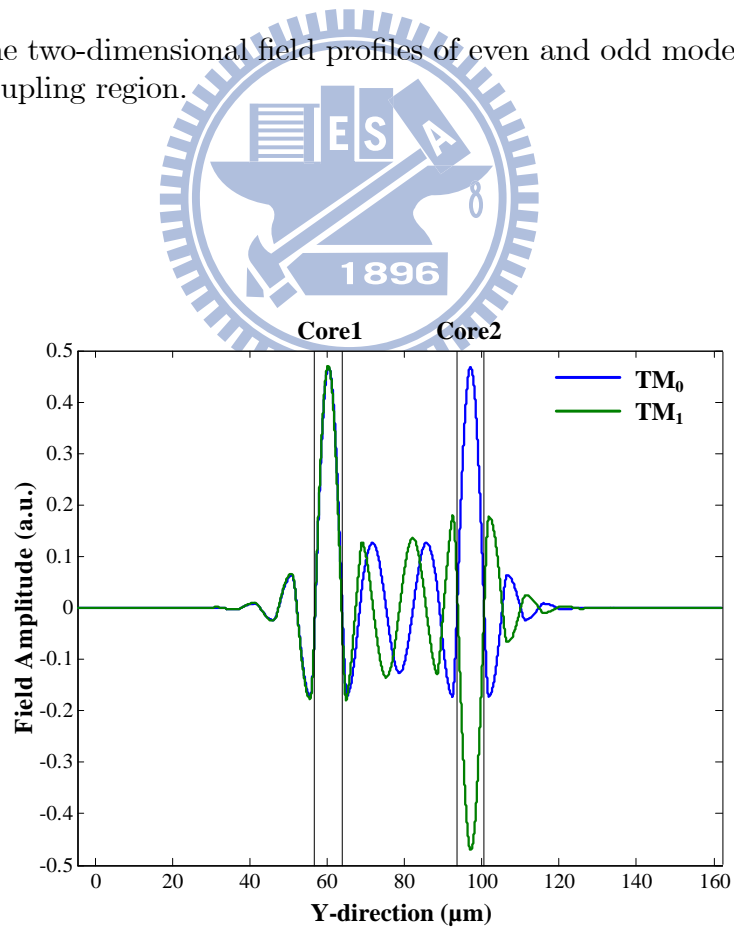
Figure 3-12: The two-dimensional field profiles of even and odd modes for TM polarization in the coupling region.

Table 3.6: The propagation losses of the first ten modes for TM polarization in the decoupling region.

Mode	Loss (dB/cm)
TM_0	0.109
TM_1	0.109
TM_2	7.7
TM_3	8.6
TM_4	5.5
TM_5	29.7
TM_6	30.6
TM_7	45.4
TM_8	63.7
TM_9	48.6
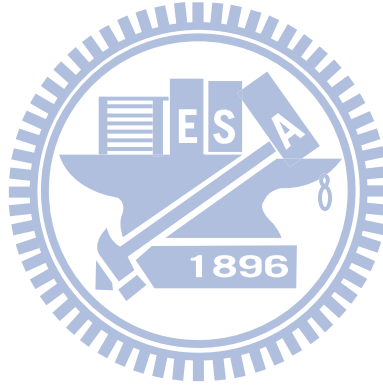
Table 3.7: The propagation losses of the first ten modes for TM polarization in the coupling region.

Mode	Loss (dB/cm)
TM_0	0.109
TM_1	0.108
TM_2	7.1
TM_3	8.4
TM_4	8.7
TM_5	29.0
TM_6	32.3
TM_7	18.1
TM_8	65.3
TM_9	58.6
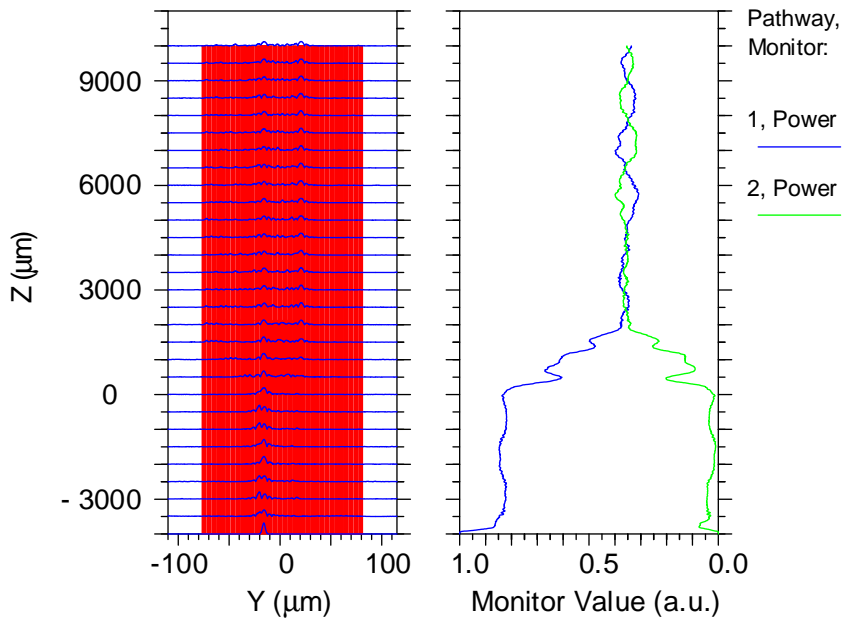
Figure 3-13: The BPM simulation result of the dual ARROW power splitter for separation width of 30 μm and the length of the coupling region of 2150 μm ($L_c/2$) when the beam launched into the left core.
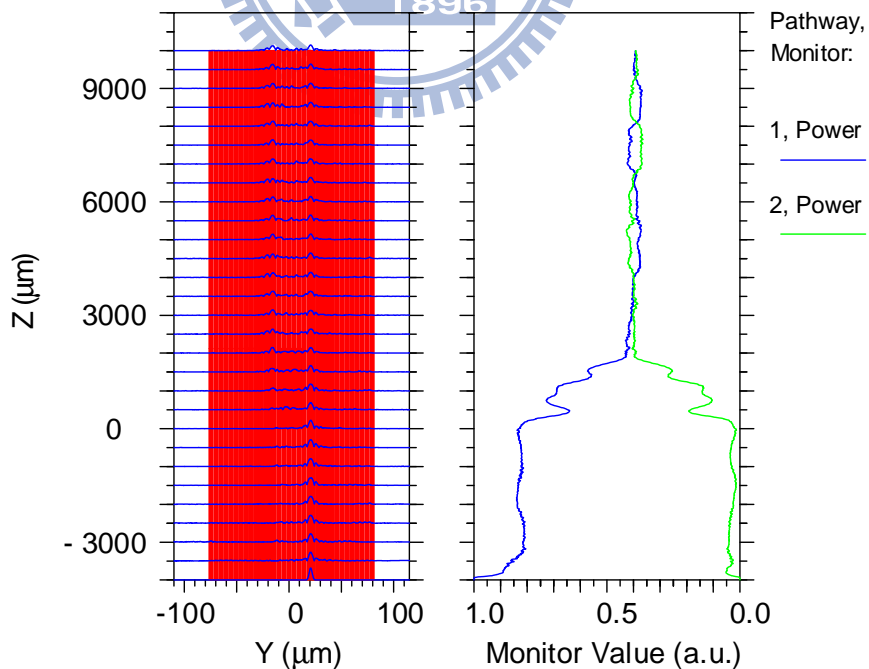
Figure 3-14: The BPM simulation result of the dual ARROW power splitter for separation width of 30 μm and the length of the coupling region of 2150 μm ($L_c/2$) when the beam launched into the right core.

31

and the decoupling region, respectively. The beam propagation method (BPM) included in the commercial software package R-soft V.5.1 was used to simulate our designed dual ARROW power splitters by launching a power into the left core or the right core. For verifying the coupling characteristics and the performances of the power splitters, we also designed and fabricated five different lengths of the coupling region as 1950, 2050, 2150, 2250, and 2350 μm as examples.

Chapter 4

Fabrication of Si-Based Dual ARROW Power Splitters

4.1 Introduction

In this chapter, we will introduce the fabrication of Si-based dual ARROW powers splitters. Our vertical ARROW structure includes three SiO_x layers (one is the core and two are the second claddings) and two amorphous silicon layers (the first cladding) in between. We used the Oxford PECVD (Plasma-Enhanced Chemical Vapor Deposition) system (STS multiplex cluster system) to deposit SiO_x layers, and the HDPCVD (High Density Plasma Chemical Vapor Deposition) system to deposit amorphous silicon layers. In addition, we used the thermal coater system to deposit aluminum to be our hard mask. After depositing all layers, the lithography and etching process were proceeded. Finally, we used the wet bench to remove the residual aluminum layer and the in-line scanning electron microscopy (in-line SEM) to inspect the fabrication process. Figure 4-1 shows the fabrication processes of the dual ARROW power splitters and the fabrications were processed in the National Nano Device Laboratories (NDL) and in Nano Facility Center at National Chiao Tung University. The detailed fabrication parameters are discussed in the following sections.

Flow Chart

(1) Deposit five layers by HDPCVD and PECVD.

(2) Deposit Al layer by Thermal Coater.

(3) Spin coat negative photoresist by Track.

(4) Pattern by Track and E-beam.

(5) Etch Al layer by Metal Etcher.

(6) Etch Oxide layer by Metal Etcher.

(7) Remove residual Al layer by Wet Bench.
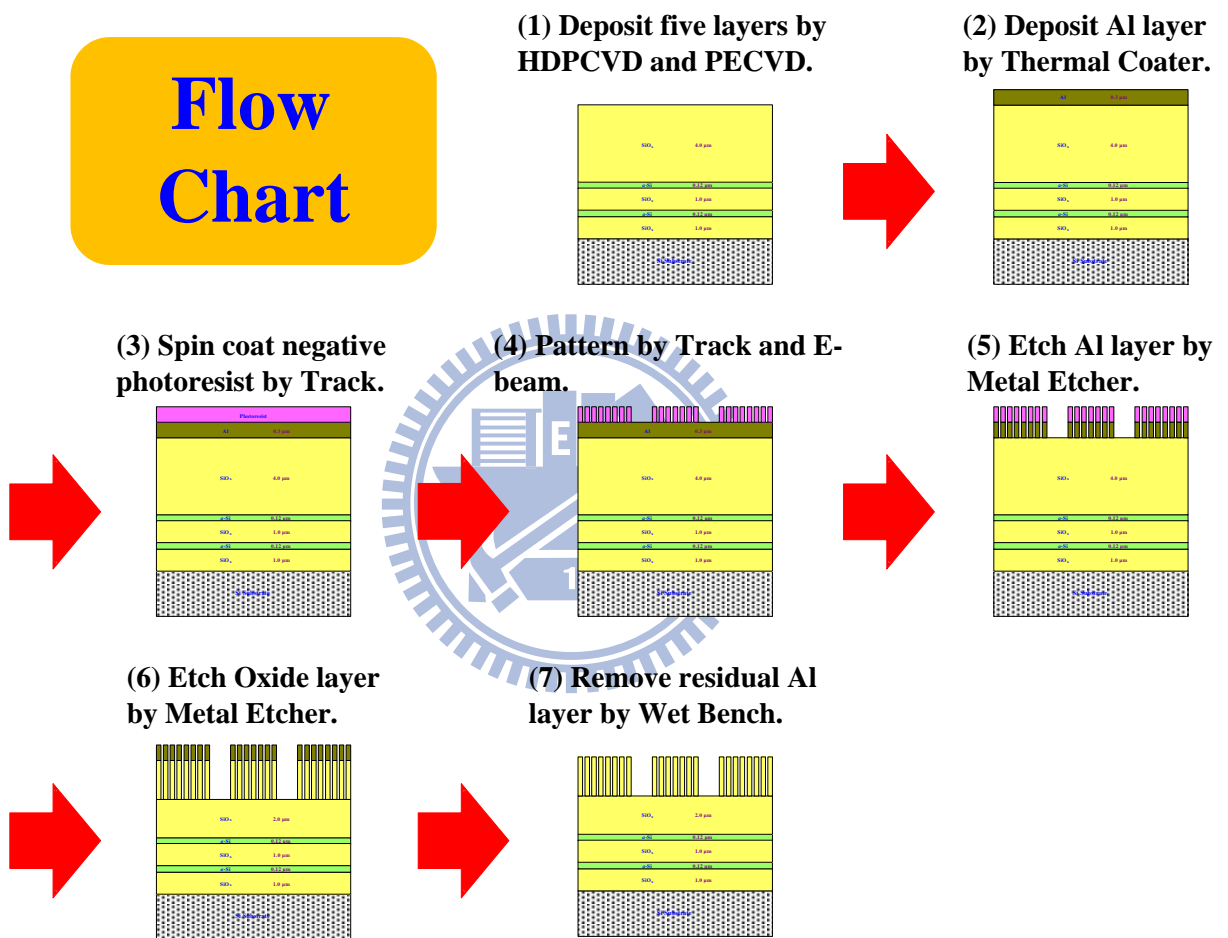
Figure 4-1: The fabrication processes of dual ARROW power splitters.

4.2 Deposition

Basically, RCA cleaning is necessary for a wafer to eliminate organic, inorganic attachment, and other contaminants. After RCA cleaning, we used the Chamber-B of the Oxford PECVD system to deposit SiOx films for the core and the second cladding layers. The PECVD system can deposit thick films with lower stress, and the deposition rate is faster than a horizontal furnace system. Moreover, the PECVD system produces oxide films with high conformality and low viscosity at a low deposition temperature.

The designed thickness of the second cladding layer is 1 μm, and the thickness of the core layer is 2 μm. The deposition parameters for 1-μm SiOx are listed in Table 4.1.

Table 4.1: Deposition parameters for 1-μm SiOx.

Time (sec)	965
RF Power (50kHz)	40
TEOS (sccm)	50
O$_2$ (sccm)	300
Pressure (mTorr)	500
Temperature (°C)	350

Then we used the HDPCVD system to deposit the amorphous silicon film (the first cladding layer) with a thickness of 0.120 μm. The chemical reaction is

$$\text{SiH}_4 \rightarrow \text{Si} + 2\text{H}_2. \tag{4.1}$$

By try and error, the better parameters were found to deposit thin films with high refractive index, low stress and good uniformity. The deposition parameters for 0.120 μm a-Si are listed in Table 4.2. Here, we repeated three times in the steps 1 to 3.

Table 4.2: Deposition parameters for 0.120-μm amorphous silicon.

Steps	1	2	3
Time (sec)	180	1	600
ICP Power (W)	0	45	45
Pressure (mTorr)	200	200	200
Ar (sccm)	50	50	50
H$_2$ (sccm)	800	800	800
SiH$_4$ (sccm)	50	50	50
Temperature (°C)	200	200	200

The thicknesses of the five points and the average refractive indices of cladding layers

35

are shown in Figure 4-2 and Table 4.3. The average thickness of the core layer was deposited as 2.07 μm. The thicknesses and the indices of each layer were measured by using "N&K analyzer 1500", it is a popular thin film measurement system based on the patented "N&K method" [27]. The method can use to calculate the thickness and the refractive index of thin films by utilizing Forouhi and Bloomer dispersion equations based on quantum mechanics.

Then we used the thermal coater system to deposit the aluminum layer with 3000 Å thickness as a hard mask. Since we expected to transfer the image from the photoresist (P.R.) to the underneath film without any critical dimension loss, therefore, a perfect etching profile is favored.
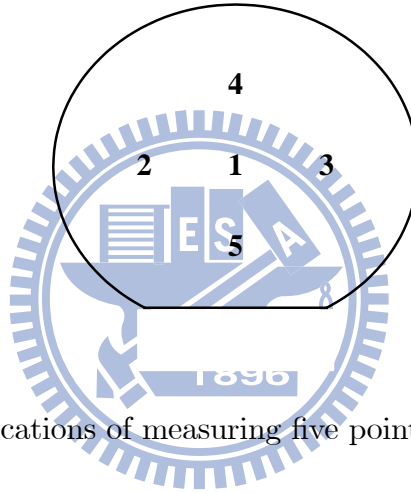
Figure 4-2: The locations of measuring five points on a 6-inch Si wafer.

Table 4.3: The thicknesses and the refractive indices of the five points of cladding layers at $\lambda = 1.55$ μm.

Material	SiOx		a-Si	
Thickness / Refractive Index	d (μm)	n	d (μm)	n
Location 1	1.13	1.455	0.123	3.85
Location 2	1.10	1.457	0.118	3.82
Location 3	1.11	1.454	0.120	3.85
Location 4	1.07	1.455	0.117	3.81
Location 5	1.13	1.457	0.119	3.84
Average	1.11	1.456	0.119	3.83

4.3 Lithography

Figure 4-3 shows the layout pattern of the dual ARROW power splitter which includes three parts: the input region, the coupling region, and the decoupling region, which was designed by R-soft and L-edit software. After completing the deposition processing steps, we used the "Clean Track MK-8" system for the lithography process. If the wafer was bended too much, the machine arm of the exposure system could not grab it. Therefore, before coating P.R., we used the stress measuring instrument to measure the radius of curvature of the wafer. The lithography procedures are described as follows:

a. Spin Coating and Soft Baking

On the wafer surface, we added the HMDS, $(CH_3)_3SiNHSi(CH_3)_3$, for enhancing the adhesion between the wafer and P.R.. The temperature is 90 °C and the baking time is 60 seconds. After cooling the wafer, the negative photoresist was applied. Initially, the speed of spin coating should be slow for the P.R. spread uniformly on the wafer surface. The spin coating speed was set as 500 rpm for 10 seconds. Then it ramps to the final speed of 5000 rpm for 45 seconds. The thickness of negative P.R. is 3800 Å.

b. Hot-plate Unit

The step was used to remove the solvent of P.R. and to enhance the adhesion between the Al and P.R. layers. The temperature of the step is 90 °C and the baking time is 90 seconds.

c. Exposure, Development and Hard Baking

The dual ARROW power splitters were patterned by the "Leica E-beam" (Leica weprint 200) with exposing dosage 4.5 μC/cm^2. We used the "Clean Track MK-8" for exposure and development. After developing, we used hard bake to harden the resin within the P.R. and stop the reaction between the developer and P.R. layers. The temperature of the step is 120 °C and the baking time is 90 seconds. Finally, we used the in-line SEM to inspect the fabrication results.
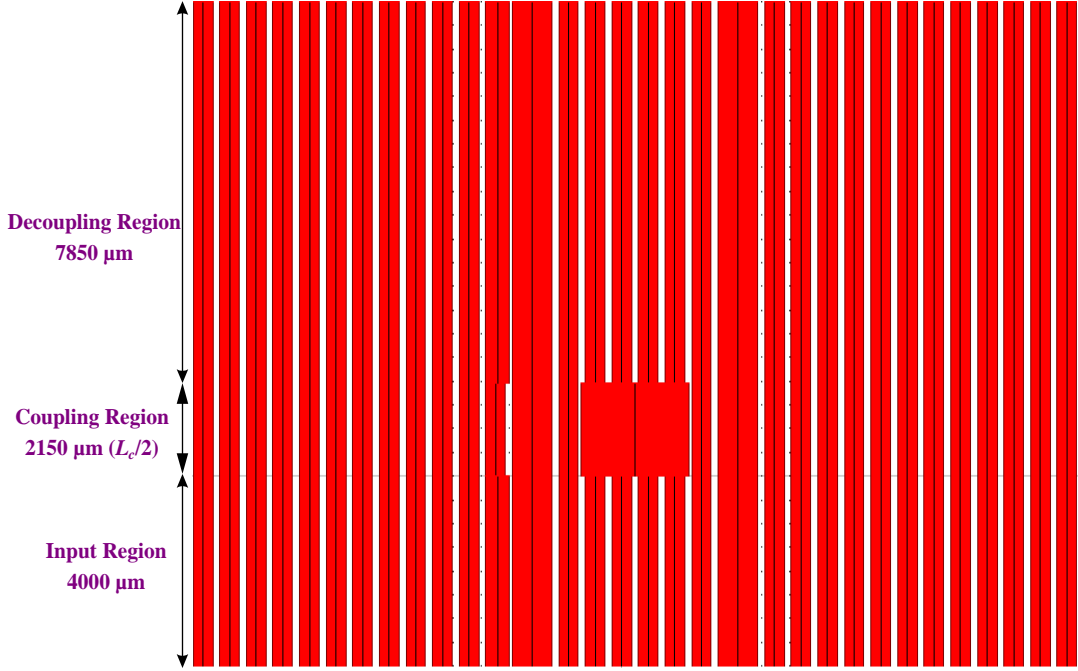
Figure 4-3: Layout diagram of the dual ARROW power splitter.

4.4 Etching Process and AEI (after etching inspection)

After completing after-develope-inspection (ADI), we used the metal etcher, "ILD-4100", for etching aluminum of 3000 Å and SiOx of 20000 Å. The etching recipes are shown in Tables 4.4 and 4.5. The etching time for aluminum of 3000 Å is about 38 seconds and for SiOx of 20000 Å is about 600 seconds.

Table 4.4: The recipe for etching aluminum 3000 Å by using metal etcher, "ILD-4100".

Steps	1	2
Time (sec)	3	35
RF Power (W)	1000	1000
Bias Power(W)	100	100
Pressure (mTorr)	5	5
Cl$_2$ (sccm)	85	100
N$_2$ (sccm)	15	0
Load Value	Auto	Auto
Tune Value	4050	4050

In the recipes, CHF$_3$ was used to produce polymers and CF$_4$ was used to produce the ions of fluorine. The ions of fluorine were used to etch the designed segment. After

Table 4.5: The recipe for etching SiOx 20000 Å by using metal etcher, "ILD-4100".

Step	1
Time (sec)	600
RF Power (W)	1000
Bias Power (W)	75
Pressure (mTorr)	4
CF$_4$ (sccm)	20
CHF$_3$ (sccm)	20
Load Value	Auto
Tune Value	3250

etching process, we used the wet-bench system to remove the residual aluminum film on the wafer with the chemical solution of H$_2$SO$_4$: H$_2$O$_2$ = 3 : 1 at 130 °C for 10 minutes. Then we used the P-10 surface profiler to meausre the depth and the in-line SEM to measure the width. After etching inspection (AEI) images were photographed by the in-line SEM.

Figures 4-4 (a) to (c) show the AEI topview SEM images of the coupling region and the decoupling region of the dual ARROW power splitters, and the average etching depth of the trench is 1.98 μm.
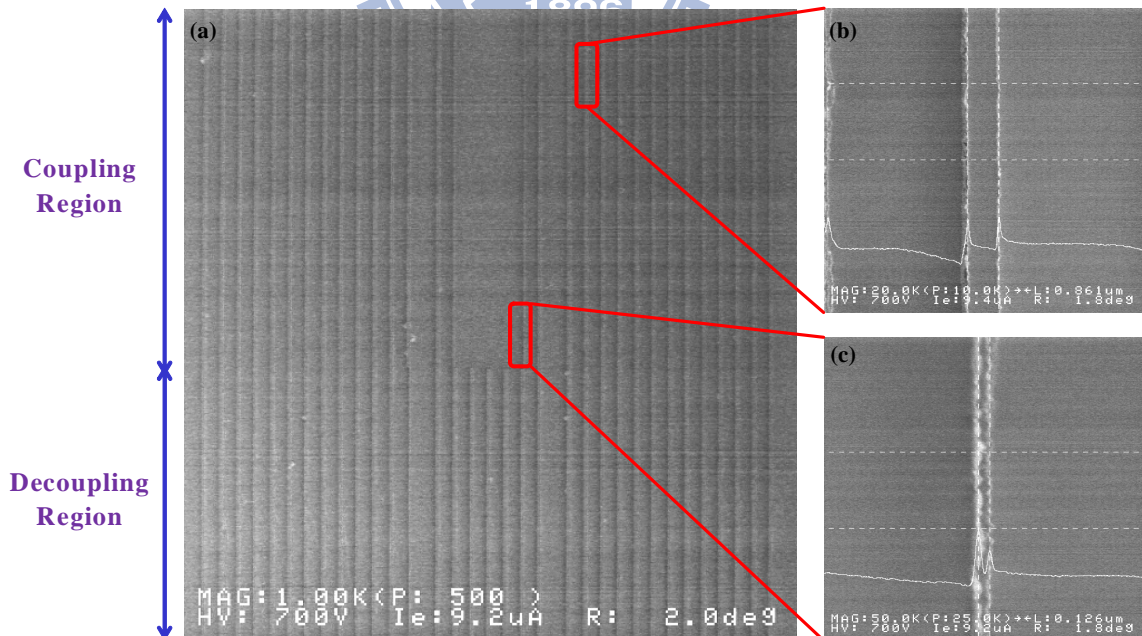
Figure 4-4: The AEI topview SEM images of (a) the dual ARROW power splitter, (b) the coupling region, and (c) the decoupling region.

Chapter 5

Characterization and Discussion

5.1 The Setup of the Optical Measurement System

After accomplishing all of the fabrication process, we used the lensed fibers coupled with the waveguide input and output in the optical measurement system to perform the experiments for characterizing the performance for our designed devices at the operation wavelength λ of 1.55 μm, and the setup is illustrated in Figures 5-1 and 5-2.

The optical measurment instruments contain:

(1) The 1.55-μm diode laser: It can be used to generate the light of λ of 1.55 μm.

(2) Lensed fibers: They are used to provide a convenient way to improve coupling between an optical fiber and a waveguide device.

(3) Optical microscope (OM): It assists the alignment of the fibers with the input and output ports of the waveguide.

(4) Infrared (IR) charge-coupled device (CCD) camera: It can view the light spot at λ of 1.55 μm, and we put a 20X lens in front of IR camera to focus the light spot.

(5) TV monitor: It can display the light spot images from the IR camera to facilitate observation and photography.

(6) Photodetector: It is used to detect and measure the optical power.

(7) Power meter: It shows the power intensity.

First, we aligned the lensed fiber with the input port of the dual ARROW waveguide. Next, we put the IR camera on the output port of the dual ARROW waveguide, and move the position of the input lensed fiber near the input port of the waveguide. At this time, we tuned the x, y, and z positions of the stage and the IR camera until two clear
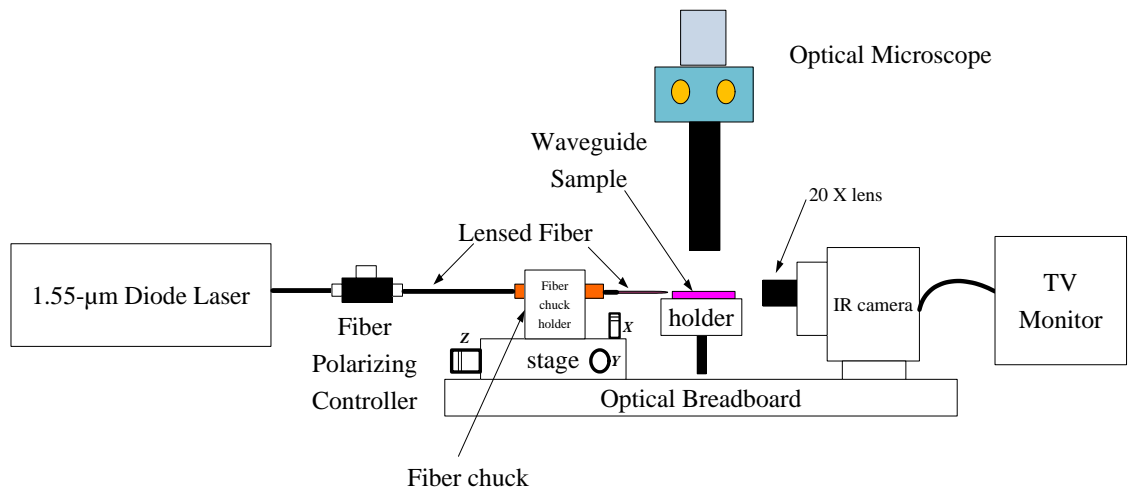
Figure 5-1: The optical measurement setup for the alignment of the input lensed fiber with the IR camera.
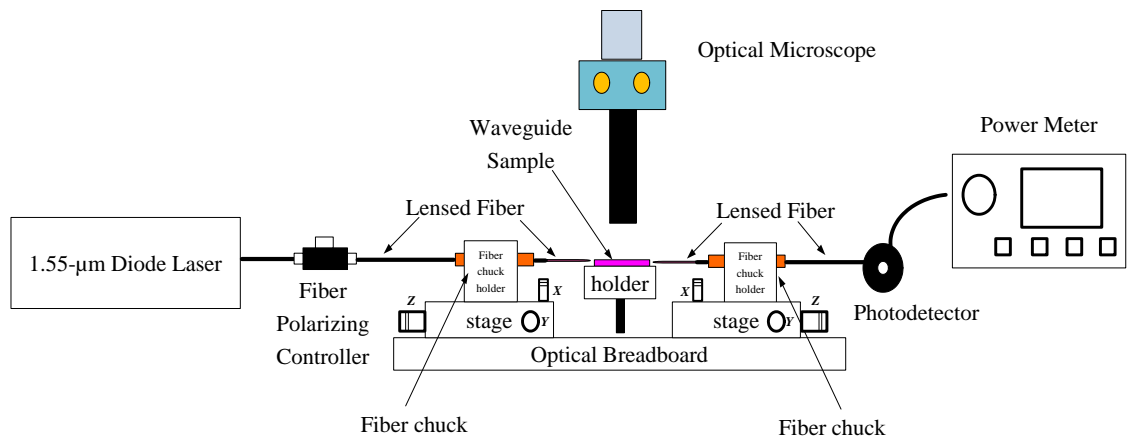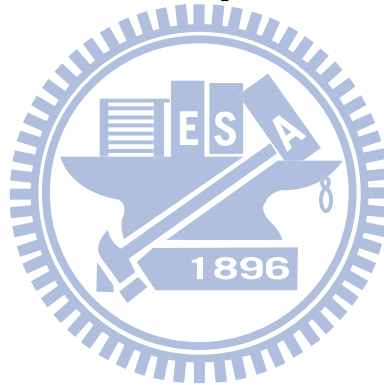
Figure 5-2: The optical measurement setup with photodetector for the power measurement.

light spot images on TV monitor were obtained, as shown in Figure 5-3. The stringent requirements for end-face flatness and alignment accuracy at the input and output of the waveguides are necessary. After we aligned the lensed fiber, we removed the IR camera and put the output lensed fiber near to the output port of the devices, as shown in Figure 5-2, and tuned the x, y, and z positions of the input and output ports stages until the power meter read a maximum value. Finally, the output power was detected by the photodetector, and the power intensity were recorded and displayed on the power meter.
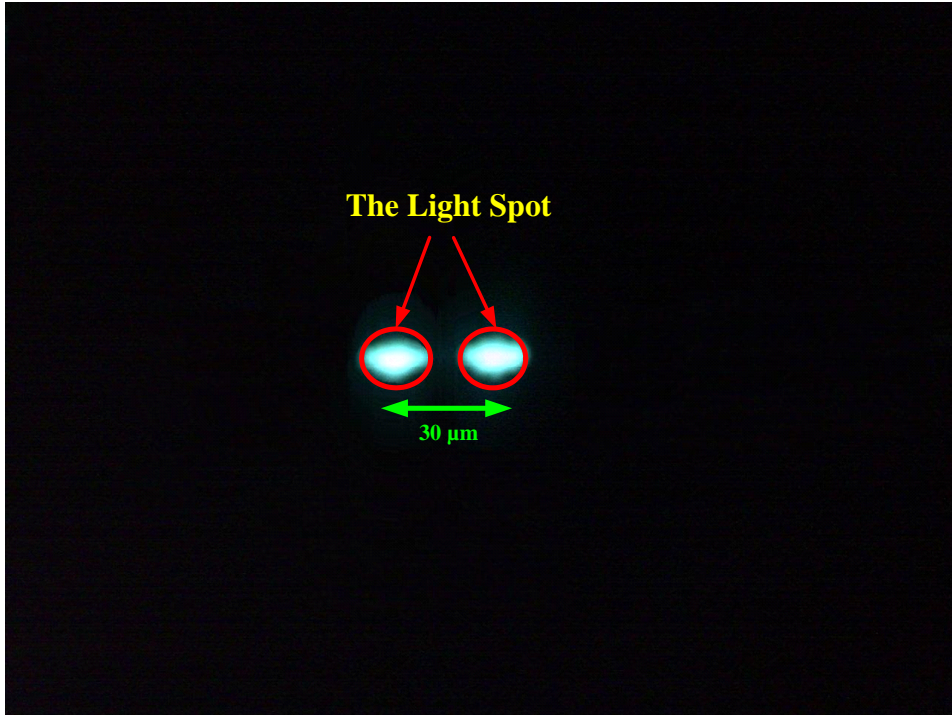
Figure 5-3: The IR camera image of the light spot from the output port of the dual ARROW power splitter with a separation width of 30 μm.

5.2 Cut-back Method for Propagation Loss of the Dual ARROW Power Splitters

For verifying the performances of the power splitters with a coupling length L_c of 4300 μm, we designed five different lengths power splitters, 1950, 2050, 2150 ($L_c/2$), 2250, and 2350 μm, and we launched a power only into the left core or only into the right core to measure the output power. In the experiment, guided waves were excited and we used

the cut-back method to measure the propagation losses of the waveguides. The method is often used for measuring the total attenuation of a waveguide device and has the advantage that a relatively accurate measurement is possible with a simple configuration, but it is a destructive method and information about mode-order dependence of losses can not be obtained. The propagation losses of the transmittances with different lengths of the device can be obtained as

$$\alpha = \frac{-10 \times \log\left(\frac{P_2}{P_1}\right)}{L_2 - L_1} \; (\text{dB/cm}), \tag{5.1}$$

where P_1, P_2 and L_1, L_2 are the transmittances and the lengths before and after cutting, respectively. Here, we define the P_1 and P_2 are the sum of P_{core1} and P_{core2} with different lengths, where P_{core1} is the output power of core 1 by launching a power only into the left core or only into the right core and P_{core2} is the output power of core 2 for launching a power only into the left core or only into the right core. The power in decibel relative to 1 mW is defined as

$$P \; (\text{dBm}) = 10 \times \log\left(\frac{P_{\text{core1}} + P_{\text{core2}}}{1 \; \text{mW}}\right). \tag{5.2}$$

We measured five samples to analyze the characteristics of the power splitters. The relations between the values of the normalized output power and the propagation lengths of the samples 1, 2, 3, 4, and 5 by launching a power only into the left core and only into the right core are shown in Figures 5-4 to 5-8. Then, the values of propagation losses from the slope of the linear fitting line were obtained. Tables 5.1 to 5.5 show the propagation losses of the samples 1, 2, 3, 4, and 5 by linear fitting in Figures 5-4 to 5-8. The results are quite consistant.

Table 5.1: The propagation loss measurement results of five samples for launching a power (a) only into the left core and (b) only into the right core, respectively. The length of the coupling region is 1950 μm.

(a)	Sample Number	1	2	3	4	5
	Propagation Loss (dB/cm)	1.92	2.89	4.99	2.26	2.42

(b)	Sample Number	1	2	3	4	5
	Propagation Loss (dB/cm)	1.96	1.76	2.01	1.18	1.24

Table 5.2: The propagation loss measurement results of five samples for launching a power (a) only into the left core and (b) only into the right core, respectively. The length of the coupling region is 2050 μm.

(a)

Sample Number	1	2	3	4	5
Propagation Loss (dB/cm)	2.39	2.94	3.26	2.88	3.48

(b)

Sample Number	1	2	3	4	5
Propagation Loss (dB/cm)	2.94	1.12	1.01	1.43	2.08

Table 5.3: The propagation loss measurement results of five samples for launching a power (a) only into the left core and (b) only into the right core, respectively. The length of the coupling region is 2150 μm ($L_c/2$).

(a)

Sample Number	1	2	3	4	5
Propagation Loss (dB/cm)	3.45	1.95	2.33	1.51	1.88

(b)

Sample Number	1	2	3	4	5
Propagation Loss (dB/cm)	2.98	1.27	1.55	2.08	1.84

Table 5.4: The propagation loss measurement results of five samples for launching a power (a) only into the left core and (b) only into the right core, respectively. The length of the coupling region is 2250 μm.

(a)

Sample Number	1	2	3	4	5
Propagation Loss (dB/cm)	1.75	1.96	2.08	2.77	2.73

(b)

Sample Number	1	2	3	4	5
Propagation Loss (dB/cm)	1.78	2.35	1.71	1.56	1.72

Table 5.5: The propagation loss measurement results of five samples for launching a power (a) only into the left core and (b) only into the right core, respectively. The length of the coupling region is 2350 μm.

(a)

Sample Number	1	2	3	4	5
Propagation Loss (dB/cm)	1.94	2.19	3.37	2.78	2.77

(b)

Sample Number	1	2	3	4	5
Propagation Loss (dB/cm)	2.56	2.33	2.34	2.05	2.58

Figure 5-4: The propagation loss for launching a power (a) only into the left core and (b) only into the right core, respectively. The length of the coupling region is 1950 μm.

Figure 5-5: The propagation loss for launching a power (a) only into the left core and (b) only into the right core, respectively. The length of the coupling region is 2050 μm.

(a)

Sample	1	2	3	4	5
Slope	-3.45	-1.95	-2.33	-1.51	-1.88

(b)

Sample	1	2	3	4	5
Slope	-2.98	-1.27	-1.55	-2.08	-1.84

Figure 5-6: The propagation loss for launching a power (a) only into the left core and (b) only into the right core, respectively. The length of the coupling region is 2150 μm ($L_c/2$).

Figure 5-7: The propagation loss for launching a power (a) only into the left core and (b) only into the right core, respectively. The length of the coupling region is 2250 μm.

(a)

Sample	1	2	3	4	5
Slope	-1.94	-2.19	-3.37	-2.78	-2.77

- Sample1
- Sample2
- Sample3
- Sample4
- Sample5
- Linear Fit of Sample1
- Linear Fit of Sample2
- Linear Fit of Sample3
- Linear Fit of Sample4
- Linear Fit of Sample5

(b)

Sample	1	2	3	4	5
Slope	-2.56	-2.33	-2.34	-2.05	-2.58

- Sample1
- Sample2
- Sample3
- Sample4
- Sample5
- Linear Fit of Sample1
- Linear Fit of Sample2
- Linear Fit of Sample3
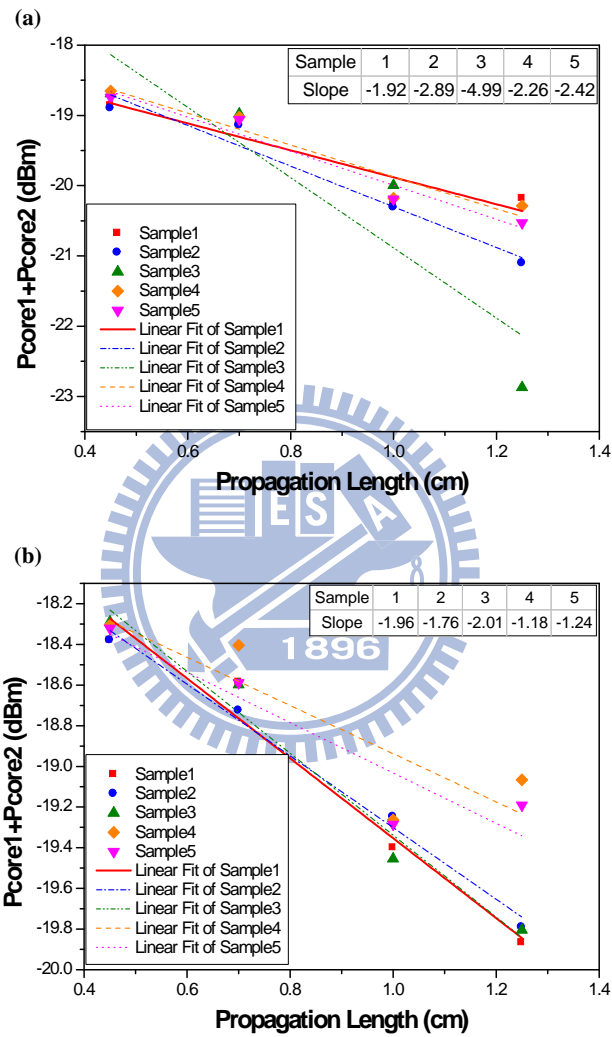- Linear Fit of Sample4
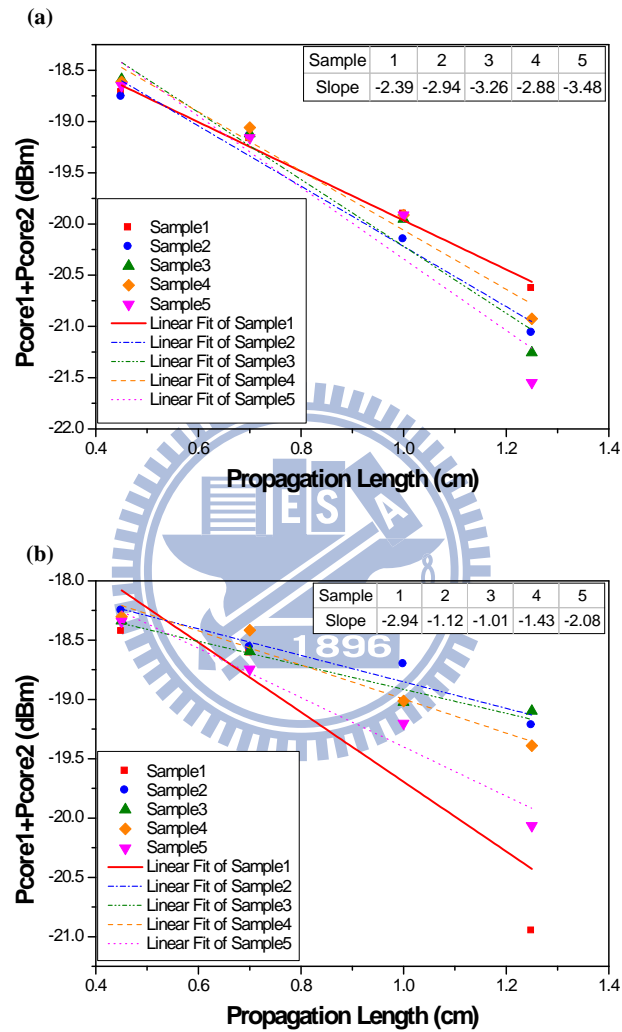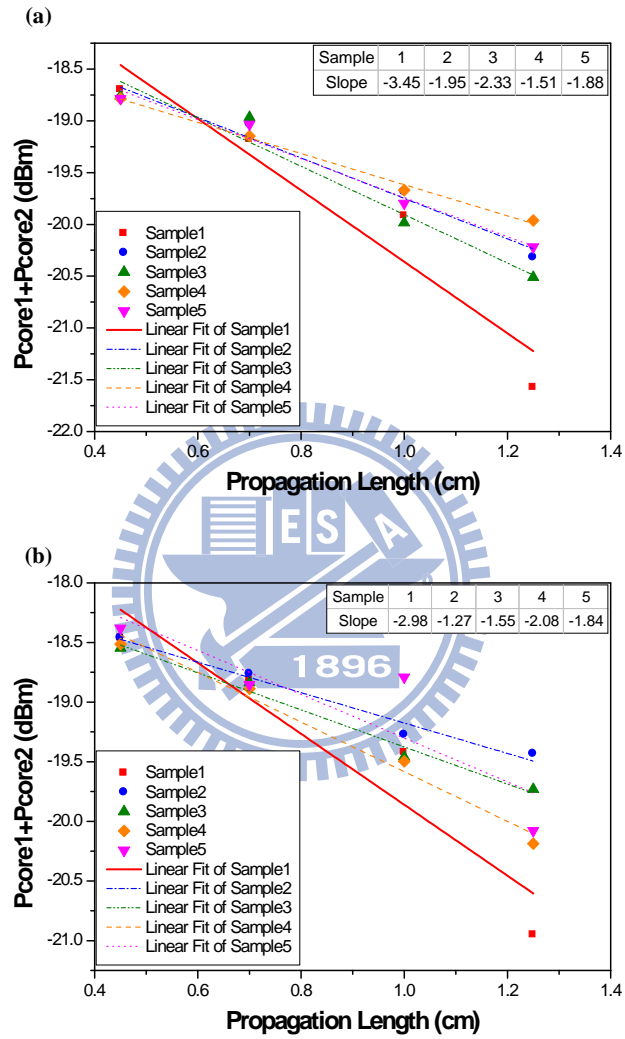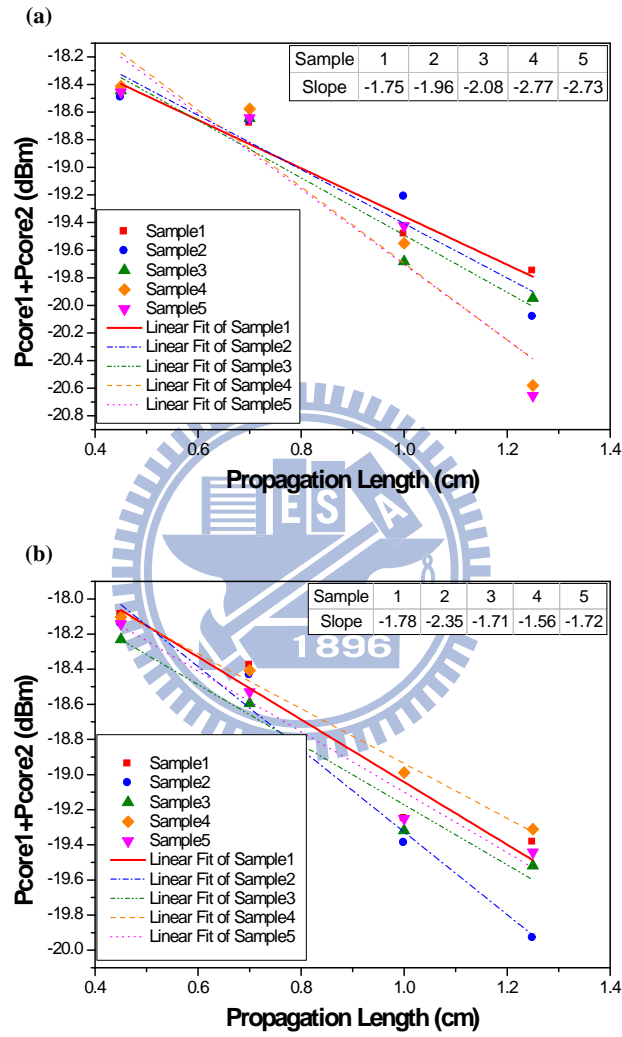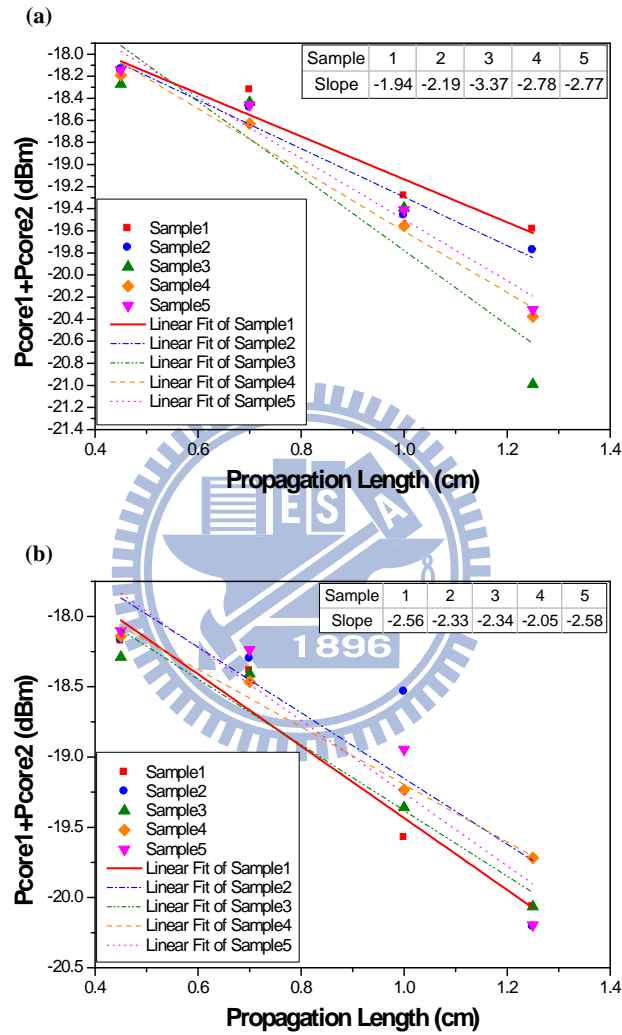- Linear Fit of Sample5

Figure 5-8: The propagation loss for launching a power (a) only into the left core and (b) only into the right core, respectively. The length of the coupling region is 2350 μm.

49

5.3 The Measurement Results of the Dual ARROW Power Splitters

For dual ARROW power splitters, the imbalance is an important parameter. The output power imbalance in dB is defined as

$$\text{imbalance} = \left| 10 \times \log \left(\frac{P_{\text{core1}}}{P_{\text{core2}}} \right) \right| , \tag{5.3}$$

where P_{core1} and P_{core2} are the output powers of core 1 and core 2 of the dual ARROW power splitters, respectively. If the value of imbalance is lower, the performance of the designed power splitter is better. Here, we separately show the imbalances by launching a power only into the left core or only into the right core. Figures 5-9 and 5-10 show the imbalance measurement results of five samples for our designed dual ARROW power splitters. Tables 5.6 and 5.7 show the measurement results of five samples for output powers of core 1 and core 2, P_{core1} and P_{core2}, and the imbalance. In Tables 5.6 and 5.7, the length of the coupling region is 2150 μm ($L_{\text{c}}/2$). The P_{core1} and P_{core2} average imbalance and standard deviation are 0.45 and 0.12 dB by launching a power into the left core of five samples, and 0.57 and 0.05 dB for launching a power into the right core.

Table 5.6: The measurement results of five samples by launching a power into the left core for output powers of core 1 and core 2, P_{core1} and P_{core2}, and the imbalance. The length of the coupling region is 2150 μm ($L_{\text{c}}/2$).

Sample Number	1	2	3	4	5
P_{core1} (μW)	6.12	8.03	6.79	8.14	6.67
P_{core2} (μW)	5.37	7.03	6.23	7.35	6.26
Imbalance (dB)	0.57	0.58	0.37	0.44	0.28

Table 5.7: The measurement results of five samples by launching a power into the right core for output powers of core 1 and core 2, P_{core1} and P_{core2}, and the imbalance. The length of the coupling region is 2150 μm ($L_{\text{c}}/2$).

Sample Number	1	2	3	4	5
P_{core1} (μW)	9.17	7.98	8.84	7.89	6.68
P_{core2} (μW)	8.02	6.91	7.93	6.88	5.84
Imbalance (dB)	0.58	0.63	0.47	0.59	0.58

Figure 5-9: The imbalance measurement result of five samples for launching a power into the left core. The length of the coupling region is 2150 μm ($L_\mathrm{c}/2$).
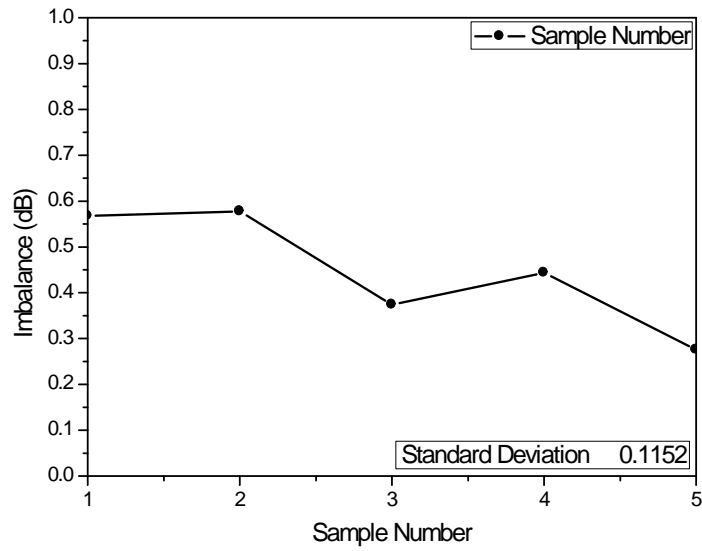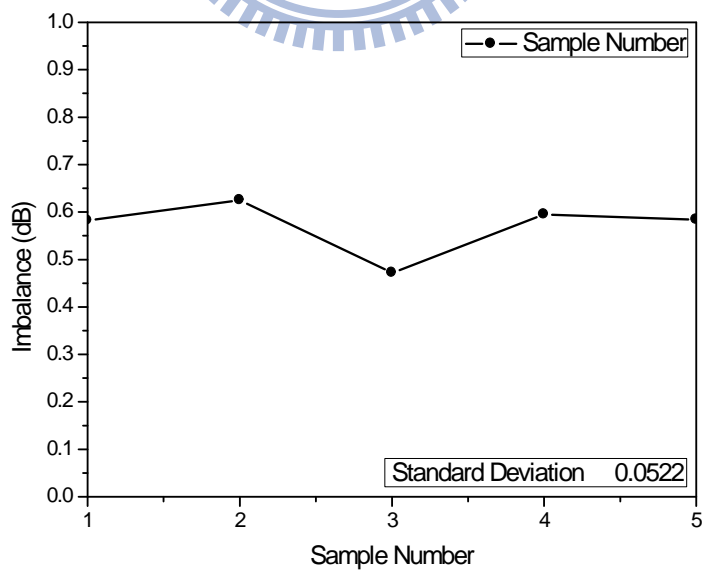

Figure 5-10: The imbalance measurement result of five samples for launching a power into the right core. The length of the coupling region is 2150 μm ($L_\mathrm{c}/2$).

Figures 5-11 and 5-12 show the relations between the normalized output power and the length of coupling region of our designed dual ARROW power splitters by launching a power into the left core and the right core, respectively. Figures 5-11(a) and 5-12(a) are the simulation results for the length of the coupling region from 150 μm to 4150 μm. Figures 5-11(b) and 5-12(b) show the simulation and measurement results of our designed dual ARROW power splitters with the length of the coupling region as 1950, 2050, 2150, 2250, and 2350 μm, respectively.

Figure 5-11: (a) The simulation results with the length of the coupling region from 150 to 4150 μm. (b) The simulation and measurement results of our designed dual ARROW power splitters for launching a power into the left core.

Figure 5-12: (a) The simulation results with the length of the coupling region from 150 to 4150 μm. (b) The simulation and measurement results of our designed dual ARROW power splitters for launching a power into the right core.

5.4 Discussion

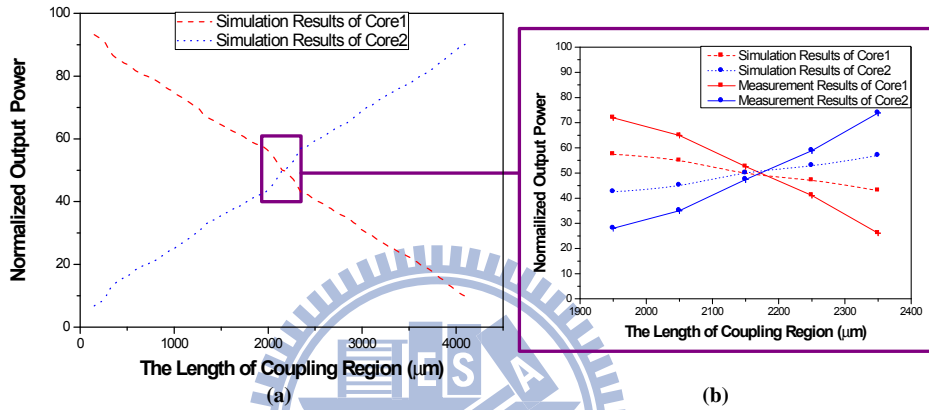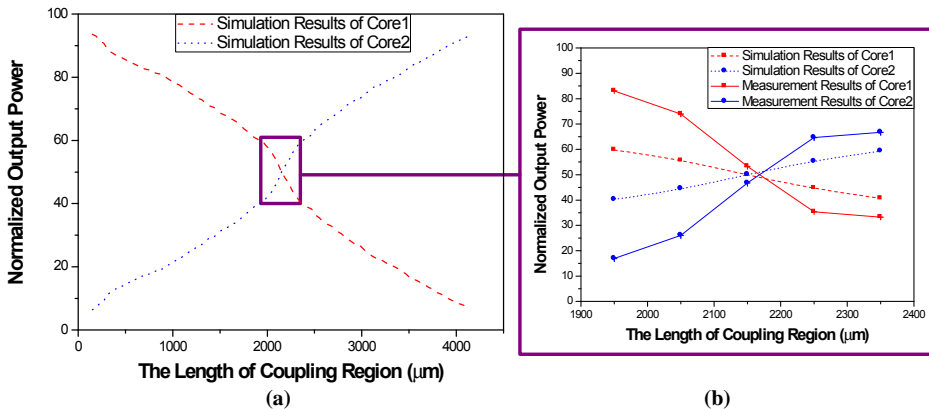In Chapter 3, the parameters of our designed devices shown in Figure are as follows: the refractive indices of $n_g/n_h/n_l/n_h/n_l$ are 1.45/3.7/1.45/3.7/1.45, the thicknesses of $d_g/d_h/d_l/d_h/d_l$ are 2.0/0.12/1.0/0.12/1.0 μm, the widths of $w_{g1}/w_{g2}/w_{h1}/w_{l1}/w_{h2}/w_{l2}/w_{h3}/w_{l3}$ are 7.0/7.0/ 1.24/3.5/0.5/4.24/0.5/19.2 μm, and the etching depth d_x is 2.0 μm. In Chapter 4, the fabrication results of the dual ARROW power splitters are as follows: the average refractive indices of SiOx and amorphous silicon are 1.46 and 3.83, the average thickness of SiOx and amorphous silicon are 1.11 and 0.12 μm, the shape of trench is trapezoid, and the average etching depth d_x is 1.98 μm. In this Chapter, the imbalance measurement results of the average imbalance are 0.45 and 0.57 dB for launching a power only into the left core and only into the right core, respectively.

From Figures 5-11 and 5-12, we can observe the measurement results and the simulation results are different. These differences between the simulation results and the measurement results of the dual ARROW power splitters arise from many possible fabrication errors. Because of the imperfection of the waveguides, the shape of the waveguide is trapezoid, as shown in Figure 4-4, w_{g1}, w_{g2}, w_{h1}, w_{l1}, w_{h2}, w_{l2}, w_{h3}, and w_{l3} are changed. Thus the length of the coupling region of our designed power splitter is changed. Moreover, when the etching depth d_x is changed, the effective indices of quasi even and odd mode are changed, so the length of the coupling region is changed accordingly. If the dual ARROW waveguides are not certainly symmetric, the radiation losses due to mode conversion from the guided modes to radiation modes of the two waveguides are different, which results in the imbalance of the power splitter. Moreover, if the densities of defects in two waveguides are different, these also affect the imbalance of the power splitter.

The measurement results of propagation losses of five samples with a length of the coupling region of 2150 μm ($L_c/2$) by launching a power only into the left core are 3.45, 1.95, 2.33, 1.51, and 1.88 dB/cm and by launching a power only into the right core are 2.98, 1.27, 1.55, 2.08, and 1.84 dB/cm, respectively. The propagation losses of the dual ARROW power splitters include [29]: (1) Absorption loss: Impurities in the dual ARROW waveguides materials result in interband absorption, and impurity absorption. (2) Scattering loss [30]-[32]: It is caused by imperfection of waveguide structure during fabrication processes, such as inclined sidewall of the guiding layer and some defects in the guiding layer. Moreover, the surface between layers is rough, which also affects

propagation losses. (3) Mode conversion loss: It is due to conversion from the excited mode to other guided modes caused by the waveguide imperfection. From the above reasons, the losses of our devices might be significantly influenced by fabrication process.

Chapter 6

Conclusion

In this thesis, design, fabrication, and characterization of Si-based dual ARROW power splitters are discussed, and we verified the performances of the power splitters with different lengths of the coupling region. In this research, we used three theories including the transfer matrix method (TMM), the effective index method (EIM), and the beam propagation method (BPM). Considering process convenience, we chose the $SiOx$ as the core layer and the second cladding layer material, and the amorphous silicon as first cladding layers, because they are commonly used materials in the commercial semiconductor process. The thickness of the core layer was chosen as 2.0 μm, and the thicknesses of the first and the second cladding layers were chosen as 0.12 μm and 1.0 μm according to the antiresonance condition, respectively.

The ARROW structure utilizes the antiresonance reflection to confine lightwaves within a low-index core layer on a high-index silicon substrate, and it can be realized by standard fabrication technology of semiconductor. Besides, in the guiding mechanism of antiresonance reflection instead of total internal reflection, the losses of high order modes are large, so the ARROW structures can be regarded as low-loss quasi-single mode waveguides. Moreover, their core index and size can be compatible with single-mode fiber index and diameter to provide efficient coupling to fibers.

Furthermore, the main advantage of an ARROW-based coupler over a conventional waveguide coupler is that ARROW's can be remotely coupled because of their nondecaying field profile inside the intermediate cladding layers. The coupling behavior between dual ARROW waveguides strongly depends on the degree of the structural symmetry. Combined with these features, the dual ARROW power splitters were designed with a

separation width of 30 μm. The coupling length is 4300 μm and the lengths of the coupling region as 1950, 2050, 2150 ($L_c/2$), 2250, and 2350 μm are fabricated to verify the coupling characteristics.

When all of the parameters of the dual ARROW power splitters were designed, the devices were fabricated by using the equipments in the National Nano Device Laboratories and the Nano Facility Center in National Chiao Tung University. Then, the optical measurement system was set up at an operating wavelength λ of 1.55 μm. The average imbalance and standard deviation are 0.45 and 0.12 dB by launching a power into the left core of five samples, and 0.57 and 0.05 dB for launching a power into the right core. The propagation losses of five samples with a length of the coupling region of 2150 μm ($L_c/2$) by launching a power only into the left core are 3.45, 1.95, 2.33, 1.51, and 1.88 dB/cm and for the right core are 2.98, 1.27, 1.55, 2.08, and 1.84 dB/cm, respectively. Measurement results show that our dual ARROW power splitters can be efficicntly realized.

In the future, it requires more rigorous simulations and analyzes based on full three-dimensional algorithms to optimize the designs. For fabrication, how to enhance the uniformity of thin film shall be emphasized. Moreover, selecting the better etching recipe will improve the etching profiles, and the coupling efficiency will be improved. Furthermore, the dual ARROW power splitter may be applied on biosensor for detecting the biomolecules.

Bibliography

[1] H. F. Taylor and A. Yariv, "Guided wave optics," *Proc. IEEE*, vol. 62, no. 8, pp. 1044–1060, Aug. 1974.

[2] D. Marcuse, "The coupling of degenerate modes in two parallel dielectric waveguides," *Bell Syst. Tech. J.*, vol. 50, pp. 1791–1816, 1971.

[3] E. A. J. Marcatili, "Dielectric rectangular waveguide and directional coupler for integrated optics," *Bell Syst. Tech. J.*, vol. 48, pp. 2071–2102, 1969.

[4] A. Yariv, "Coupled mode theory for guided–wave optics," *IEEE J. Quantum Electron.*, vol. QE-9, no. 9, pp. 919–933, Sep. 1973.

[5] A. Hardy and W. Streifer, "Coupled mode theory of parallel waveguides," *IEEE J. Lightwave Technol.*, vol. LT-3, no. 5, pp. 1135–1146, Oct. 1985.

[6] M. A. Duguay, Y. Kokubun, T. L. Koch, and L. Pfeiffer, "Antiresonant reflecting optical waveguides in SiO₂-Si multilayer structures," *Appl. Phys. Lett.*, vol. 49, no. 1, pp. 13–15, Jan. 1986.

[7] L. B. Soldano and E.C. M. Penning, "Optical multi-mode interference devices based on self-imaging: principles and applications," *IEEE J. Lightwave Technol.*, vol. 13, no. 4, pp. 615–627, Apr. 1995.

[8] M. Mann, U. Trutschel, C. Wachter, L. Leine, and F. Lederer, "Directional coupler based on an antiresonant reflecting optical waveguide," *Opt. Lett.*, vol. 16, no. 11, pp. 805–807, June 1991.

[9] T. Baba, Y. Kokubun, T. Sakaki, and K. Iga, "Loss reduction of an ARROW waveguide in shorter wavelength and its stack configuration," *IEEE J. Lightwave Technol.*, vol. LT-6, no. 9, pp. 1440–1444, Sep. 1988.

[10] S.-H. Hsu and Y.-T. Huang, "Design and analysis of Mach-Zehnder interferometer sensors based on dual strip antiresonant reflecting optical waveguide structures," *Opt. Lett.,* vol. 30, no. 21, pp. 2897–2899, Nov. 2005.

[11] T. Tamir (Ed.), *Guided-wave optoelectronics,* Springer-Verlag, 1990.

[12] R. M. Knox and P. P. Toulios, "Integrated circuits for millimeter through optical frequency region," in *Proc. MRI Symp. Submillimeter Waves,* J. Fox, Ed., Brooklyn: Ploytechnic Press, pp. 497–516, 1970.

[13] K. Okamoto, *Fundamentals of Optical Waveguides,* Academic Press, 2000.

[14] W.H. Press, S.A. Teukolsky, W.T. Vetterling and B.P. Flannery, *Numerical Recipes in Fortran 77 : The Art of Scientific Computing,* Chapter 19, Cambridge University Press, New York, 1996.

[15] H. J. W. M. Hoekstra, G. J. M. Krijnen, and P. V. Lambeck, "On the accuracy of the finite difference method for applications in beam propagation techniques," *Opt. Commun.,* vol. 94, pp. 506–507, 1992.

[16] H. J. W. M. Hoekstra, G. J. M. Krijnen, and P. V. Lambeck, "New formulation of the beam propagation method based on the slowly varying envelop approximation," *Opt. Commun.,* vol. 97, pp. 301–303, 1993.

[17] G. R. Hadley, "Transparent boundary condition for beam propagation," *Opt. Lett.,* vol. 16, no. 9, pp. 624–626, May 1991.

[18] G. R. Hadley, "Multistep method for wide-angle beam propagation," *Opt. Lett.,* vol. 17, no. 24, pp. 1743–1745, Dec. 1992.

[19] E. A. J. Marcatili, "Dielectric rectangular waveguide and directional coupler for integrated optics," *Bell Syst. Tech. J.,* vol. 48, no. 9, pp. 2071–2102, 1969.

[20] K.S. Chiang, "Dual effective-index method for the analysis of rectangular waveguides," *Appl. Opt.,* vol. 25, pp. 2169–2174, 1986.

[21] W. P. Huang, A. Nathan, R. M. Shubair, and Y. L. Chow. "The modal characteristics of ARROW structures," *IEEE J. of Lightwave Technol.,* vol. 10, no. 8, pp. 1015–1022, 1992.

[22] J.-J. Deng, "Analysis and design of antiresonant reflecting optical waveguide devices with discontinuities," Ph. D. Dissertation, National Chiao Tung University, Hsinchu, Taiwan, R.O.C., 2000.

[23] T. Baba and Y. Kokubun, "New polarization-insensitive antiresonant reflecting optical waveguide (ARROW-B)," *IEEE Photon. Technol. Lett.*, vol. 1, no 8, pp. 232–234, 1989.

[24] Y.-H. Chen and Y.-T. Huang, "Coupling-efficiency analysis and control of dual antiresonant reflecting optical waveguides," *IEEE J. Lightwave Technol.*, vol. 14, pp. 1507–1513, June 1996.

[25] Y. Suematsu and K. Kishino, "Coupling coefficient in strongly coupled dielectric waveguides," *Radio Science*, vol. 12, no. 4, pp. 587–592, July–Aug. 1977.

[26] A. Ferreras, F. Rodríguez, E. Gómez-Salas, J. L. de Miguel, and F. Hernández-Gil, "Useful formulas for multimode interference power splitter/combiner design," *IEEE Photon. Technol. Lett.*, vol. 5, no. 10, pp. 1224–1227, Oct. 1993.

[27] A. R. Forouhi and I. Bloomer, "Optical dispersion relations for amorphous semiconductors and amorphous dielectrics," *Phys. Rev. B*, vol. 34, no. 15, pp. 7018–7026, Nov. 1986.

[28] A. R. Forouhi and I. Bloomer, "Optical dispersion relations of crystalline semiconductors and dielectrics," *Phys. Rev. B*, vol. 38, no. 3, pp. 1865–1874, July 1988.

[29] H. Nishihara, M. Haruna, and T. Suhara, *Optical integrated circuits.* McGraw-Hill, 2001.

[30] T. Baba and Y. Kokubun, "Scattering loss of antiresonant reflecting optical waveguides," *IEEE J. Lightwave Technol.,* vol. 9, no. 5, pp. 500–597, 1991.

[31] P. Singer, "Furnaces Evolving to Meet Diverse Thermal Processing Needs," *Semiconductor International,* p. 85, Mar. 1997.

[32] SEMATECH, "Furnace Equipment Overview," module 3 in *Furnace Processes and Related Topics,* pp. 3–6.

Vita

Ming-Shun Hsu was born in Miaoli, Taiwan on July 27, 1987. He received the B.S. degree in Department of Electronic Engineering from I-Shou University of Education in June 2009. He entered the Institute of Electronics, National Chiao Tung University (NCTU) in September 2009. His major studies is optics communications and micro electro mechanical devices fabrication and measurement. He received the M.S. degree from NCTU in June 2011.